Towards Self-Powered Tunable Mechanical Oscillators: A Conceptual Study

Masoud Rezaei[1], Michael I Friswell[2], Wei-Hsin Liao[1*]

[1]Department of Mechanical and Automation Engineering, The Chinese University of Hong Kong, Shatin, NT, Hong Kong, China

[2]Faculty of Science and Engineering, Swansea University, Bay Campus, Fabian Way, Crymlyn Burrows, Swansea SA1 8EN, United Kingdom

Abstract:

Mechanical oscillator resonance frequencies are of paramount importance and determine their performance from different perspectives such as bandwidth, vibration mitigation, and energy harvesting. As active tuning is hindered by energy consumption, this research investigates comprehensively for the first time if the inherent energy of a vibrating oscillator can supply the required energy to alter its natural frequency. To investigate the viability of this concept, a nonlinear partially covered piezoelectric beam-based oscillator with a full bridge rectifier and magnetic tuning mechanism under base excitation is considered, and its geometrically nonlinear model is derived. First, an approximate solution is proposed to study the capacitor charging process in steady-state excitation. Then, numerical integration and the multi-harmonic harmonic balance method (HBM) with pseudo-arclength continuation are exploited to investigate the nonlinear dynamics, mechanical response, and external capacitor voltage of the self-powered tunable oscillator (SPTOS). To investigate the sufficiency of the SPTOS energy for tuning, the required energy for different levels of change in the SPTOS natural frequency are obtained. It is found that the SPTOS can supply the energy to significantly change its natural frequency. The capacitor charging time and generated energy depend on the ratio of external capacitance to internal capacitance. The SPTOS efficiency under chirp excitation is then investigated, and the results show that both the chirp rate and the capacitance ratio affect the capacitor energy. Finally, by comparing the maxima of energy for the steady-state and chirp excitations, it is shown that the SPTOS energy in the former case is considerably higher than the latter case. Thus, the SPTOS can make larger changes in its frequency when excited in a steady-state scenario.

Keywords: Self-powered tunable oscillator; Magnetic actuation; Energy recovery; Nonlinear vibration; Harmonic excitation; Harmonic balance method; Cyclic-fold bifurcation

* Corresponding author
Email address: whliao@cuhk.edu.hk (Wei-Hsin Liao)

1- Introduction

A mechanical oscillator that is represented by a linear or nonlinear mass-spring-damper, is a fundamental component of any vibrating system including structures, machines, sensors, resonators, actuators and so on. In different applications, an oscillator may play different roles, but in many cases, tuning the resonance frequencies of oscillators is of crucial importance and directly affects the performance of the system. Some examples are vibration absorbers, rotating machines, and energy harvesters. Specifically, to ensure the maximum vibration mitigation, the resonance frequency of an absorber should be tuned to match the vibration frequency of the host structure, whose vibrations need to be suppressed. To reduce unbalanced rotating machinery vibration, the rotor resonance frequency must be located away from the excitation frequency. In energy harvesting applications, the resonance frequency of an energy harvester must be tuned to coincide with the environmental excitation frequency to harvest the maximum energy; otherwise, the harvested energy level is very small. Accordingly, tuning an oscillator resonance frequency is of great importance. To achieve this, active and semi-active [1, 2] approaches are promising but they either require an actuation mechanism or tuning mechanism that both need an external energy source. Also, these tuning methods are complex and costly. In addition, owing to the external energy requirement, their application is often not justifiable in some cases, for example energy harvesting, because the expended energy would be higher than the harvested energy.

As oscillators are vibrating systems with considerable energy, the question arises whether the vibration energy of the oscillator, whose frequency is required to be tuned, can be used to supply the required energy for tuning? If yes, how much of the required energy can be supplied by the oscillator? To address these questions, this research investigates the concept of exploiting the inherent energy of a vibrating oscillator to power its frequency tuning mechanism. Essentially, this idea is similar to energy harvesting, which is a family of techniques used to convert environmental energies from different sources including, but not limited to, vibrations [3, 4], fluid-solid interactions [5, 6], human motion [7], and acoustic [8], to small-scale electrical energy. Furthermore, environmental energy can be converted to electrical energy via different approaches such as piezoelectric (PZT), electromagnetic, and electrostatic [9, 10]. However, due to the scalability, high energy density, and broad working frequency of piezoelectric materials, they have been widely used for energy harvesting.

Different research efforts have been devoted to improving the modeling aspects of energy harvesters. Friswell et al. [11] investigated energy harvesting from a vertically mounted PZT beam with a tip mass and under base excitation. The results show that the system is highly nonlinear and exhibits a range of complex responses. The most efficient case was observed to be the pre-bucked case, having a low resonance frequency, wider bandwidth, and higher power. Tripplet et al. [12] investigated the role of nonlinear electromechanical coupling and found that it can affect the power prediction in a PZT energy harvester. Tang and Wang [13] investigated the effects of tip mass offset on the performance of a PZT energy harvester with an elastic magnifier. The eigenvalue analysis and frequency response curves show that the tip mass geometry can significantly affect the harvested energy through resonant frequency and strain distribution. Mam et al. [14] theoretically and experimentally investigated the validity of a PZT energy harvester model by considering both geometric and electrical nonlinearities under transverse and parametric excitations. The results show that under transverse excitation, nonlinear effects are significant even for low amplitudes. On the other hand, parametric excitation is only effective for large amplitudes. Khorshidi et al. [15] observed that for a functionally graded (FG) energy harvester under base excitation, increasing the FG index results in an increased voltage. In addition, performance enhancement of energy

harvesters has been pursued by many researchers and mainly lies in exploiting nonlinear behaviors. Zhang et al. [16] investigated an asymmetric tri-stable piezoelectric–electromagnetic energy harvester exposed to colored noise, and found that correlation time, electromechanical coupling, and time constant ratios determine the harvester performance. Also, the hybrid system generates more power than the individual transduction mechanism. Fan et al. [17] used a specific design to introduce internal resonance in a PZT energy harvester and found that this enhances bandwidth.

Nevertheless, the target of energy harvesting is usually powering sensors, and this is the key difference between conventional energy harvesting and this research. Furthermore, some criteria such as charging time and the ultimate use of the energy are not considered in pure energy harvesting studies. The application of system energy recovery, that is sought in this research, will mean different concepts are studied, which will be discussed throughout this paper. Limited research has been conducted in the use of system energy to control structures. For example, Bryant et al. [18] experimentally investigated the potential of a piezoelectric flow energy harvester to power a DC motor to actuate an aerodynamic control surface. The harvested energy was able to deflect a flap through a specific mechanism. However, no mathematical model was derived for further investigations and the response of the airfoil was not studied. The idea of simultaneous energy harvesting and vibration mitigation via dual-purpose linear and nonlinear absorbers have been studied extensively [19-21], but the harvesting and suppression modules were independent and the harvested energy was not used for actuation purposes.

Reviewing the literature, it is shown that despite a great deal of research that has been conducted on energy harvesting for wireless sensing, along with notably fewer works for other applications, no research has investigated the potential of vibration energy to realize self-powered tunable oscillators. To address this knowledge gap, this research investigates the idea of a self-powered tunable oscillator (SPTOS), using numerical, analytical, and approximate-analytical techniques. The motivation of the current approach is that, although many publications exist in the field of piezoelectric energy harvesting, based the authors' knowledge, there is no comprehensive research that studies the potential of recovering the system energy to achieve a tunable oscillator, which is the focus of our research. First, an oscillator, energy converting mechanism, and tuning approach are defined. The conversion mechanism, that acts as a bridge between the inherent energy of the system and the required energy for tuning, can be an electromechanical transduction mechanism. Due to the mentioned advantages of piezoelectric materials and their minimum interference with the host system oscillations compared to other transducers, which is of crucial importance for the SPTOS, the system of oscillator and transduction mechanism is chosen to be a doubly-clamped bimorph beam consists of a substrate layer which is covered by piezoelectric patches and driven by harmonic base excitation. This structure plays the role of the oscillator whose frequency needs to be tuned and where energy can be extracted. Using a PZT material to recover energy also reduces the interference of the energy conversion mechanism with the oscillator performance, as opposed to sizeable mechanisms such as electromagnetic transduction. In addition, the tuning mechanism is chosen to be a magnetic device where a magnetic force is applied to the beam to alter its stiffness, and in turn, its resonance frequency. The energy harvesting circuit is connected to an external capacitor via a full bridge rectifier to convert AC voltage to DC in order to store the energy. First, the dimensionless geometrically nonlinear model of the bimorph oscillator under a sinusoidal base excitation and nonlinear magnetic force is derived in Section 2. Two different scenarios of steady-state harmonic and chirp excitations will be considered for the base excitation. The approximate-analytical solution for charging the external capacitor

is given in Section 3. To assess the performance of the SPTOS, the dynamical response of the system in both time and energy domains is investigated in Section 4. Finally, the conclusions are given in Section 5.

2- Nonlinear electromechanical model

2-1- Partial differential equations of the SPTOS

The schematic of the self-powered tunable oscillator (SPTOS) is shown in Fig. 1. The oscillator is a bimorph beam that is comprised of an aluminum substrate layer and four Macro Fiber Composite (MFC) piezoelectric layers partially covering its surface. Furthermore, two magnets are attached to the midpoint of the bimorph, and they interact with two external stationary magnets located at a separation distance d_v from the initial position of the moving magnets, and this acts as the magnetic actuator for frequency tuning. The whole system is driven by harmonic base excitation with amplitude a_b and frequency Ω. Two scenarios will be considered for the excitation, which are steady-state frequencies and chirp excitation. In this paper, subscripts *s*, *p*, and *m* denote the substrate layer, the PZT layer, and the magnet, respectively.

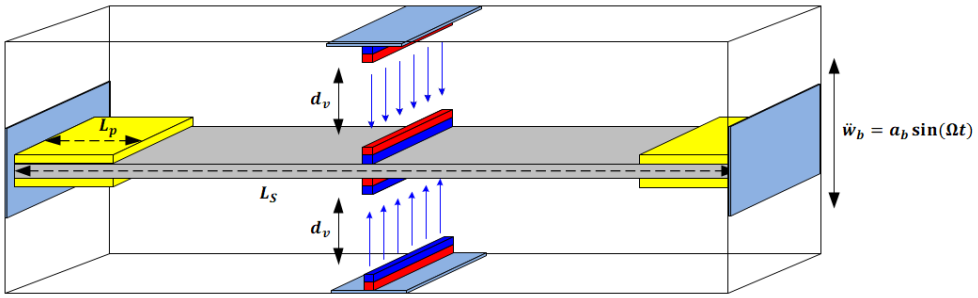

Fig. 1 Schematic of the self-powered tunable oscillator with a magnetic actuator under sinusoidal base excitation

Table 1. Geometrical and material properties of the SPTOS

Parameter (symbol)	Value (unit)	Parameter	Value (unit)
Substrate length (L_s)	9 cm	PZT Young's modulus (Y_p)	15.86 GPa
PZT length (L_p)	4 cm	Dimensionless damping ratio (ζ_1)	0.01
Substrate width (W_s)	1 cm	PZT strain constant (d_{31})	-170 pm/V
PZT width (W_p)	1 cm	Permittivity of PZT (e_{33})	19.36 nF/m
Substrate thickness (t_s)	0.2 mm	Magnet mass (m_m)	2.2 g
PZT thickness (t_p)	0.3 mm	Magnet volume (V_m)	10*10*3 mm^3
Substrate mass density (ρ_s)	7800 kg/m^3	Magnetic moment density (M)	0.96×10^6 A/m
PZT mass density (ρ_p)	5440 kg/m^3	Free-space permittivity (μ_0)	$4\pi \times 10^{-7}$ Tm/A
Substrate Young's modulus (Y_s)	212 GPa		

The length, width, and thickness of the layers are denoted by L, W and t, respectively. All PZT patches are identical, and the magnets are chosen such that their widths are the same as the bimorph width. As the bimorph is composed of three sub-sections, for further mathematical analysis, the lengths of the subsection from left to right are denoted as L_1, L_2, and L_3, respectively, where $L_1 = L_3 = L_p$ and $L_2 = L_s - (L_1 + L_3)$. In the formulation, the left and right PZT layers on the upper surface are labeled as 1 and 2. Likewise, the left and right layers on the bottom surface are labeled as 3 and 4. The dimensions and physical properties of the system are given in Table 1.

Next, by formulating the kinetic and potential energies of the electromechanical oscillator, as well as the work done by conservative and non-conservative forces, the governing equations of the oscillator vibrations are extracted utilizing the extended Hamilton's principle, which states:

$$\int_{t_1}^{t_2} (\delta T - \delta U + \delta W_{\mathrm{c}} + \delta W_{\mathrm{nc}}) \mathrm{d}t = 0 \tag{1}$$

where T and U are the total kinetic and potential energies of the system, respectively. W_c and W_{nc} are the work done by the conservative and non-conservative forces, respectively; the conservative force is the magnetic actuation force. Furthermore, t_1 and t_2 are the lower and upper limits of integration time and δ denotes the variational operator.

To derive the geometrically nonlinear model governing the system that accounts for large displacements and rotations, a Cartesian coordinate system *XYZ* is attached to the root of the beam and a local coordinate $\xi\eta\zeta$ is attached to the beam cross-section. The unit vectors along *X*, *Y*, and *Z* axes are denoted by $\mathbf{i}_{\mathrm{x}}$, $\mathbf{i}_{\mathrm{y}}$, and $\mathbf{i}_{\mathrm{z}}$ and the unit vectors along ξ, η, and ζ axes are denoted by $\mathbf{i}_1$, $\mathbf{i}_2$, and $\mathbf{i}_3$. Throughout this paper, vectors are denoted by boldface. Using these coordinate systems, the deformed configuration of an element of the bimorph is shown in Fig. 2a. The position vector of an arbitrary point of the beam after a deformation is shown by the vector $\mathbf{R}_{\mathrm{b}}$. Furthermore, the cross-section of the bimorph, neutral axis (*n.a*), and its associated dimensions are shown in Fig. 2b.

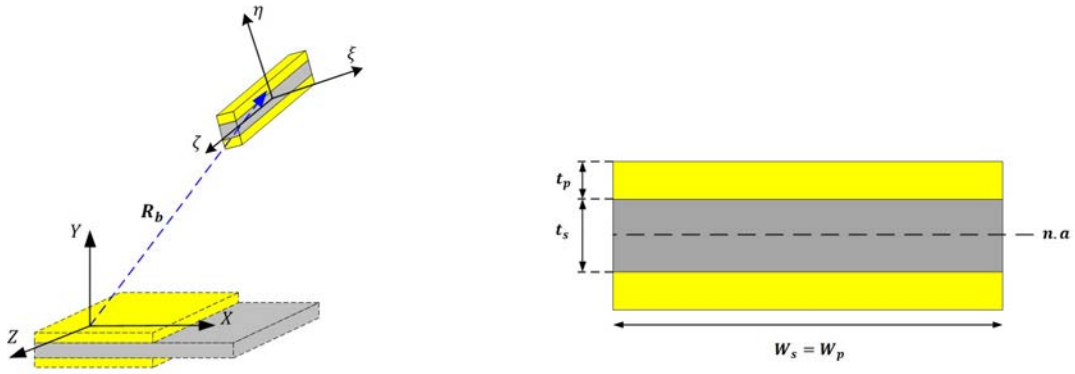

(a) (b)

Fig. 2 The bimorph: (a) deformed configuration of an element (b) cross-section

Considering a reference point on an observed cross-section in the undeformed configuration that is located at (s, y), the position vector $\mathbf{R}_{\mathrm{b}}$ of this point in the deformed configuration is:

$$\mathbf{R}_{\mathrm{b}} = \big(s + u(s,t)\big)\mathbf{i}_{\mathrm{x}} + \big(w_b(t) + w(s,t)\big)\mathbf{i}_{\mathrm{y}} + y\mathbf{i}_2 \tag{2}$$

where $u(s,t)$ and $w(s,t)$ are displacement components in the *X* and *Y* directions, respectively. Furthermore, assuming that the upper and bottom magnets act as point-masses attached at positions $(s^*, t_s/2)$ and $(s^*, -t_s/2)$, respectively, their associated position vectors are defined as:

$$\begin{aligned}\mathbf{R}_{\mathrm{mu}} &= u(s^*,t)\mathbf{i}_{\mathrm{x}} + \big(w_b(t) + w(s^*,t)\big)\mathbf{i}_{\mathrm{y}} + \frac{t_s}{2}\mathbf{i}_2 \\ \mathbf{R}_{\mathrm{mb}} &= u(s^*,t)\mathbf{i}_{\mathrm{x}} + \big(w_b(t) + w(s^*,t)\big)\mathbf{i}_{\mathrm{y}} - \frac{t_s}{2}\mathbf{i}_2\end{aligned} \tag{3}$$

Using the position vectors of the beam reference point and magnets, the variation of the beam kinetic energy can be written as [22]:

$$\begin{aligned}\delta T = -\int_0^{L_{\mathrm{b}}} [&\Big(\big(m_{\mathrm{s}} + 2m_{\mathrm{p}}[H_L + H_{\mathrm{R}}]\big)\ddot{u} + 2m_{\mathrm{m}}\ddot{u}^*\delta(s-s^*)\Big)\,\delta u \\ &+ \Big(\big(m_{\mathrm{s}} + 2m_{\mathrm{p}}[H_{\mathrm{L}} + H_{\mathrm{R}}]\big)(\ddot{w} + \ddot{w}_b) + 2m_m(\ddot{w}^* + \ddot{w}_b)\delta(s-s^*)\Big)\,\delta w]\mathrm{d}s\end{aligned} \tag{4}$$

Here, m_s is the substrate mass per unit length, m_p is the PZT layer mass per unit length, and m_m is the magnet mass. In addition, δ is Dirac's delta function and is used to write the magnet kinetic energy in integral form, L_b is the bimorph length, and H_L and H_R are Heaviside functions used for the PZT layers to define their location in the integrations. The Heaviside functions are defined as

$$H_{\mathrm{L}} = [H(s) - H(s - L_1)] \quad ; \quad H_{\mathrm{R}} = [H(s - L_1 - L_2) - H(s - L_{\mathrm{b}})] \tag{5}$$

In addition, as rigid-body translations and rotations do not yield any strain, local displacements with respect to the deformed coordinate system are used to derive fully nonlinear strain-displacement relationships. Hence, it is assumed that $\xi\eta$ is attached to the observed cross-section, and then the local displacement vector is [23]:

$$\mathbf{U} = \Big(u_1^0(s,t) - y\theta_3(s,t)\Big)\mathbf{i}_1 + u_2^0(s,t)\mathbf{i}_2 \tag{6}$$

Here, u_1^0 and u_2^0 are the displacement components of the point on the reference line and θ_3 is the rotation angle with respect to the ζ axis. As the displacement is local with respect to the $\eta\zeta$ plane, the local strain in the $\mathbf{i}_1$ direction is obtained as:

$$\epsilon_{11} = e - y\rho_3 \tag{7}$$

where ϵ_{11} is the reference point local strain in the $\mathbf{i}_1$ direction, e is the reference line strain ($\partial u_1^0/\partial s$), and ρ_3 is the bending curvature about the ζ axis ($\partial\theta_3/\partial s$). The equations relating displacement components, axial strain, and rotation angle are given in the Appendix.

To derive the oscillator potential energy, it is assumed that PZT layers 1 and 2 are connected in series, PZT layers 3 and 4 are connected in series, and layer 2 is connected to layer 3 in series. Also, the poling directions of layers 1 and 2 are in the positive Y direction and the poling direction of layers 3 and 4 are in the negative Y direction. The constitutive equations of substrate and PZT layers are given in the Appendix. Using the strain field and constitutive equations, the variation of the bimorph potential energy, which is composed of the substrate and PZT layers elastic potential energies and the PZT layers electrical potential energy, is [22]:

$$\delta U = \iiint \sigma_{11_s} \delta \epsilon_{11_s} \mathrm{d}V_s + \sum_{i=1}^{4} \iiint \sigma_{11_{\mathrm{pi}}} \delta \epsilon_{11_{\mathrm{pi}}} \mathrm{d}V_{\mathrm{pi}} \tag{8}$$

where the first volume integral is the variation of the substrate layer potential energy and the second term is the variation of the PZT layers potential energy, embracing both their elastic and electrical potential energies. In Eq. (8), $\mathrm{d}V_s$ and $\mathrm{d}V_{\mathrm{pi}}$ are the differential volume elements of the substrate layer and *i-th* PZT layer, respectively. Using the relationships in the Appendix, the variational potential energy can be rewritten as:

$$\delta U = \int_0^{L_b} \{(YAe)'(T_{11}\delta u' + T_{12}\delta w') - (YI\rho_3 + \theta V_s)'\delta\theta_3\}\mathrm{d}s + (YI\rho_3 + \theta V_s)\delta\theta_3|_0^{L_b} \tag{9}$$

In Eq. (9), T_{11} and T_{12}, the elements of the transformation matrix relating deformed and undeformed configurations, and are defined in the Appendix. YA, YI, and θ are also defined in the Appendix.

The problem has two dependent variables, namely u and w, and as implied by relationships (A.1) and (A.8), and θ_3 depends on u and w. Thus, the variational non-conservative work comes from viscous damping in the u and w directions and is defined as:

$$\delta W_{\mathrm{nc}} = -\int_0^{L_b} (c_1 \dot{u}\delta\dot{u} + c_2 \dot{w}\delta\dot{w})\mathrm{d}s \tag{10}$$

where c_1 and c_2 are the dimensional viscous damping coefficients in the u and w directions, respectively.

2-1-1 Magnetic actuation

To assess the performance of the SPTOS concept, magnetic actuation is chosen as the actuation technique. However, it must be highlighted that there are a variety of techniques for vibration control, and each of them has its own pros and cons. There are also other aspects regarding the actuation, and therefore, before formulating the magnetic interaction, first some discussions will be given on the actuation.

In terms of actuation method, there are a variety of options. For instance, conventional techniques, such as variable axial load [24, 25], have been used to control the stiffness, but their implementation in practical applications is questionable. Later, smart materials-based approaches, such as piezoelectric actuators, have been proposed and shown to be promising. Although they have a large actuation force and fast response, they are limited to a lower stroke and their resilience in harsh environments, such as high temperature applications, is challenging. Shape memory alloy (SMA) actuators offer a large stroke, but they require a complex control algorithm because they are susceptible to metallic phase changes at a specific temperature [26, 27]. Among different techniques, magnetic-based actuation has been shown to be promising and has found many applications in different forms such as non-contact actuation [28] and soft-magnetic materials [29], owing to its endurance in harsh conditions, excellent controllability, and simpler design. Non-contact magnetic actuation, which is widely applied, including the one exploited in this research, and others such as magnetic bearing [30], is a promising method mainly because of its straightforwardness in changing actuation strength using position or magnetic field.

However, closed-loop positioning may need to be incorporated to sense and feedback the SPTOS deflection and determine the position of the actuators for the desired change in the frequency. Another

concern is the response speed which may lead to a delay in tuning. It is directly related to the speed of the magnet motion during the tuning period, and thus the desired power. Nevertheless, it should be noted that this research only seeks to answer the fundamental question if the inherent energy is sufficient to power a general magnetic actuation, based on the calculated required work.

The magnetic actuation effect that tunes the oscillator stiffness enters into the equations through the conservative work. To derive the magnetic actuation force, the upper and lower external magnets are labeled as 1 and 4, respectively, and the upper and lower magnets on the bimorph are labeled as 2 and 3, respectively. The repelling force between each pair of interacting magnets tunes the stiffness. Assuming an initial gap g_0 between the upper magnets (1 and 2) as well as the lower magnets (3 and 4) and by considering a dipole-dipole interaction model [8, 31], the force between pair (1 and 2) and pair (3 and 4) after moving the external magnets towards the beam magnets by a value of x can be formulated as:

$$\mathbf{f}_{12} = -\frac{3\mu_0 m_1 m_2}{2\pi(g_0 - x)^4}\mathbf{i}_{\mathrm{y}} \quad ; \quad \mathbf{f}_{34} = \frac{3\mu_0 m_3 m_4}{2\pi(g_0 - x)^4}\mathbf{i}_{\mathrm{y}} \tag{11}$$

where $\mathbf{f}_{12}$ is the force vector between magnets 1 and 2 and $\mathbf{f}_{34}$ is the force vector between magnets 3 and 4**.** μ_0 is the free space permeability and m_i is the magnetic moment of the *i-th* magnet, which is obtained by multiplying the magnetic moment density and magnet volume. In this research, the magnets are assumed to be repulsive ($m_1 m_2 > 0$ and $m_3 m_4 > 0$). Considering that the external magnets 1 and 4 are respectively displaced towards the beam magnets 2 and 3 through an equal incremental displacement dx, the required incremental work done is:

$$\mathrm{d}W_T = \mathbf{f}_{12}.\left(-\mathrm{d}x\mathbf{i}_{\mathrm{y}}\right) + \mathbf{f}_{34}.\left(\mathrm{d}x\mathbf{i}_{\mathrm{y}}\right) \tag{12}$$

Assuming all of the magnets are identical and hence substituting m_i with m_1, by integrating the incremental work from zero to an arbitrary displacement x, and upon introducing a change of variable $d_v = (g_0 - x)$, the total magnetic work due to the magnetic actuation can be formulated as:

$$W_T = \frac{\mu_0 m_1^2}{\pi}\left(\frac{1}{d_v^3} - \frac{1}{d_{\mathrm{v0}}^3}\right) \quad ; \quad d_{\mathrm{v0}} = d_v(x = 0) = g_0 \tag{13}$$

Since $d_v < d_{\mathrm{v0}}$, the total work W_T due to the magnetic actuation is positive, as expected. By defining the dimensionless parameter $D = d_v/t_s$, in which t_s is the substrate layer thickness, the magnetic actuation force can be written in terms of the dimensionless parameter D as:

$$W_T = \frac{\mu_0 m_1^2}{\pi t_s^3}\left(\frac{1}{D^3} - \frac{1}{D_0^3}\right) \quad ; \quad D_0 = g_0/t_s \tag{14}$$

Next, once the external magnets are located at d_v, they apply a permanent magnetic actuation and tune the oscillator frequency. To model the magnetic actuation, or equivalently the magnetic stiffness, the forces between the upper pair and lower pair when the external magnets are fixed at the gap value of d_v and the oscillator is vibrating are needed. Using the dipole-dipole model, the applied dynamical force (time-dependent) from the external magnets onto the beam magnets are:

$$\mathbf{F}_{12} = -\frac{3\mu_0 m_1^2}{2\pi(d_v - w^*)^4}\mathbf{i}_{\mathrm{y}} \quad ; \quad \mathbf{F}_{34} = \frac{3\mu_0 m_1^2}{2\pi(d_v + w^*)^4}\mathbf{i}_{\mathrm{y}} \tag{15}$$

To distinguish between these dynamical (time-dependent) forces and those static forces ($\mathbf{f}_{12}$ and $\mathbf{f}_{34}$), the dynamical forces are shown by uppercase boldfaces. In Eq. (15), w^* denotes the deflection of the beam

where the magnets are attached, which is the midpoint of the beam, i.e., $w^* = w(0.5L_b, t)$. Using Taylor's series and expanding $\mathbf{F}_{12}$ and $\mathbf{F}_{34}$ about $w^* = 0$, the total magnetic actuation force on the oscillator can be represented as the following nonlinear force:

$$\mathbf{F}_{\text{mag}} \cong -\frac{\mu_0 m_1^2}{\pi d_v^4}\left(12\left(\frac{w^*}{d_v}\right) + 60\left(\frac{w^*}{d_v}\right)^3\right)\mathbf{i}_y \tag{16}$$

Considering a variational displacement vector $\delta\mathbf{w}^*$, the variational conservative force due to the magnetic actuation can be formulated as:

$$\delta W_c = -\frac{\mu_0 m_1^2}{\pi d_v^4}\int_0^{L_b}\left(12\left(\frac{w^*}{d_v}\right) + 60\left(\frac{w^*}{d_v}\right)^3\right)\delta(s - s^*)\delta w \mathrm{d}s \tag{17}$$

where Dirac's delta function δ is used to write the integral form of the variational conservative force.

Now, introducing Eqs. (4), (9), (10), and (17) into the extended Hamilton's principle and eliminating θ_3, the partial derivative equations governing the system are found as:

$$\begin{aligned} &m_b\ddot{u} + 2m_m\delta(s - s^*)\ddot{u}^* + c_1\dot{u} - (YAu')' = \left[YA\left(\tfrac{1}{2}w'^2 - u'w'^2\right)\right]' + [w'(YI(w' - \\ &u'w')')' - 2u'w'(YIw'')']' + (\theta'w')'V_s - \left[\theta'w'\left(w'^2 + 2u' - 3u'^2\right)\right]'V_s \end{aligned} \tag{18}$$

$$\begin{aligned} &m_b(\ddot{w} + \ddot{w}_b) + 2m_m(\ddot{w}^* + \ddot{w}_b)\delta(s - s^*) + c_2\dot{w} + (YIw'')'' + C_m\left[12\left(\tfrac{w^*}{d_v}\right) + \right. \\ &\left.60\left(\tfrac{w^*}{d_v}\right)^3\right]\delta(s - s^*) = \left[YA\left(u'w' - u'^2w' + \tfrac{1}{2}w'^3\right)\right]' + \left[[YI(u'w')']'(1 - u') + \right. \\ &\left.(YIw'')'\left(u' - u'^2 + w'^2\right) - \left[YI\left(u'^2w' - \tfrac{1}{3}w'^3\right)'\right]'\right]' - \theta''V_s + (\theta'u')'V_s - \left[\theta'\left(-w'^2 + \right.\right. \\ &\left.\left.\tfrac{3}{2}u'w'^2 + u'^2 - u'^3\right)\right]'V_s \end{aligned} \tag{19}$$

The associated boundary conditions are given in the Appendix. In Eqs. (18) and (19), the total mass per unit length of the substrate and PZT layers is shown by m_b. As Eq. (18) shows, for the current configuration of PZT layers, the voltage terms in the longitudinal equation of motion only contain nonlinear coefficients, which are small and imply that linear longitudinal vibrations do not produce any significant voltage. The physical reason is that during linear longitudinal vibrations, all layers experience the same strain and due to the opposite poling of the upper and lower layers, their voltages cancel out each other. However, for nonlinear vibrations, the nonlinear terms, which contain the lateral deflection, can generate voltage.

For a slender beam, the longitudinal natural frequencies are much higher than the lateral natural frequencies, and consequently, u is mainly excited by w [23]. In addition, in Eq. (18), the terms proportional to *YI* are negligible and due to the small value of the electromechanical coupling terms, the terms proportional to voltage are also negligible. Accordingly, Eq. (18) yields [32]:

$$(YIu')' = \left(\frac{1}{2}YAw'^2\right)' \tag{20}$$

Integrating Eq. (20) over the length of the beam gives:

$$u' = -\frac{1}{2}w'^2 + \frac{c(t)}{YA} \tag{21}$$

where $c(t)$ is an unknown time-dependent function. Applying the geometric boundary conditions in the longitudinal direction, $c(t)$ is found to be:

$$c(t) = \frac{\overline{YA}}{2}\int_0^{L_b} w'^2 \mathrm{d}s \qquad ; \quad \frac{1}{\overline{YA}} = \frac{L_1 + L_3}{Y_s A_s + 2Y_p A_P} + \frac{L_2}{Y_s A_s} \tag{22}$$

Using Eq. (22) in Eq. (21), it is found that:

$$u' = -\frac{1}{2}w'^2 + \frac{1}{2}\frac{\overline{YA}}{YA}\int_0^{L_b} w'^2 \mathrm{d}s \tag{23}$$

Equation (23) relates the longitudinal and lateral vibrations and shows that $u = O(w^2)$. This equation is used to reduce the number of equations of motion from two to one. Hence, by inserting Eq. (23) into Eq. (19) and keeping up to cubic terms in w, neglecting the terms proportional to *YI* and also neglecting the nonlinear electromechanical coupling terms, the equation governing the lateral vibrations is:

$$\begin{aligned} &m_b(\ddot{w} + \ddot{w}_b) + 2m_m(\ddot{w}^* + \ddot{w}_b)\delta(s - s^*) + c_2\dot{w} + (YIw'')'' + C_m\left[12\left(\frac{w^*}{d_v}\right) + \right. \\ &\left. 60\left(\frac{w^*}{d_v}\right)^3\right]\delta(s - s^*) - \left[\frac{\overline{YA}}{2}w'\int_0^{L_b} w'^2 \mathrm{d}s\right]' + \theta'' V_s = 0 \end{aligned} \tag{24}$$

In Eq. (24), which is an integro-differential equation, the nonlinear integral term is a cubic nonlinearity resulting from the midplane stretching effect.

The coupled electrical equation governing the SPTOS electrical circuit can be obtained using either the extended Hamilton's principle or Gauss's law, and the latter is exploited in this research. For the current bimorph, the PZT layers are connected in series, and each PZT layer can be regarded as a pair of parallel current source i_p and capacitor C_p, and therefore in total, four such pairs are connected in series. In addition, a full bridge rectifier (FBR), composed of four diodes, is connected to the output terminal of the PZT layers and converts the AC harvested voltage to a DC voltage using forward and reverse biasing roles to store the voltage in the external capacitor. The stored voltage/energy can be used to supply power to the magnetic actuator and tune the oscillator frequency. The schematic of the electrical circuit is shown in Fig. 3.

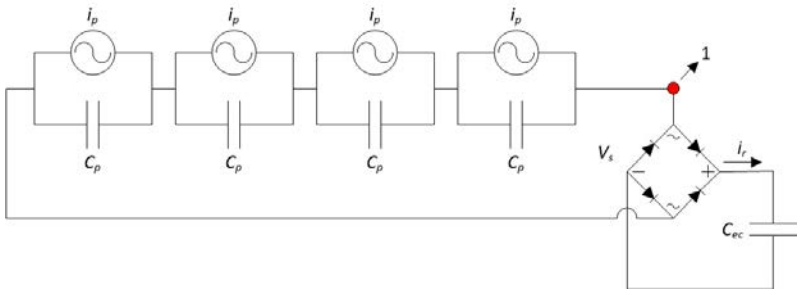

Fig. 3 The schematic of the SPTOS coupled electrical circuit with the full bridge rectifier

Applying the Gauss's law to a PZT layer in the case of no external load and FBR gives:

$$\frac{\mathrm{d}}{\mathrm{d}t}\int_A \mathbf{D}.\mathbf{n}\,\mathrm{d}A = 0 \tag{25}$$

where $\mathbf{D}$ is the electric displacement vector, $\mathbf{n}$ is the unit outward normal vector to the electrode area, and A is the electrode area. Considering one of the PZT layers, e.g. layer 1, the electric displacement and unit vector are:

$$\mathbf{D}_2 = \left(d_{31}Y_p\epsilon_{11} + \bar{\varepsilon}^s{}_{33}\left(-\frac{V_s}{4t_p}\right)\right)\mathbf{i}_\mathrm{y} \quad ; \quad \mathbf{n} = \mathbf{i}_\mathrm{y} \tag{26}$$

where $\bar{\varepsilon}^s{}_{33}$ is the piezoelectric permittivity constant at constant strain. Inserting Eq. (26) into Eq. (25) gives:

$$\frac{\bar{\varepsilon}^s{}_{33}W_pL_1}{4t_p}\dot{V}_s + d_{31}Y_pW_p\left(\frac{t_s+t_p}{2}\right)\int_0^{L_1}\dot{w}''\,\mathrm{d}s = 0 \tag{27}$$

By introducing:

$$C_p = \frac{\bar{\varepsilon}^s{}_{33}W_pL_1}{t_p} \quad ; \quad \chi = -d_{31}Y_pW_p(\frac{t_s+t_p}{2}) \tag{28}$$

Equation. (27) gives:

$$\frac{C_p}{4}\dot{V}_\mathrm{s} - \chi\int_0^{L_1}\dot{w}''\,\mathrm{d}s = 0 \tag{29}$$

In terms of Kirchhoff's current law, the second term of Eq. (29) states that a PZT layer can be considered as a current source. Now, when the FBR is forward biased and passes the current i_r, the external capacitor is in parallel with the four PZT current source-capacitor pairs. Thus, by writing Kirchhoff's current law at the node labeled 1 in Fig. 3, the circuit equation in the case of the FBR is:

$$\frac{C_p}{4}\dot{V}_s + C_\mathrm{ec}\dot{V}_s - \chi\int_0^{L_1}\dot{w}''\,\mathrm{d}s = 0 \tag{30}$$

where the first and second terms in Eq. (30) are the current passing through the internal (for the PZT layer) and external capacitors, respectively.

2-2- Discretized and dimensionless equations of SPTOS

In this research, dimensionless equations will be used to study the proposed idea in a general form. Galerkin's discretization method will be applied to discretize the system and obtain the associated ordinary differential equations (ODEs), and then the dimensionless ODEs will be obtained. It is preferred to use the bimorph fundamental frequency as a characteristic frequency to drive dimensionless time and make the dimensionless frequency of the bimorph equal to unity. As the oscillator is tunable, its first mode is of interest in this research. Specifically, for beams with cubic nonlinearities, given the excitation frequency is in the vicinity of the beam first natural frequency, a good approximation may be obtained using a discretization based on the linear first mode [23, 33]. So, although accuracy may be improved using more degrees of freedom, a good understanding on the dynamics of the system, that is sufficient for the current problem, is obtained from the single degree of freedom approximation. Therefore, the lateral bimorph deflection $w(s,t)$ is separated in space and time domains as:

$$w(s,t) = \varphi(s)q(t) \tag{31}$$

where $\varphi(s)$ is the first mode shape of the bimorph beam and $q(t)$ is its associated temporal function. As shown in the schematic diagram of Fig. 1, the oscillator is a composite beam comprised of a substrate layer and four partial piezoelectric patches covering its surface. Moving from the left to right, sub-sections 1 and 3 are sandwich parts composed of a substrate and two piezoelectric layers and sub-section 2 is the sole substrate layer. Performing the separation of variables on each sub-section of the uniform, linear, undamped, and unforced PDE governing the beam, the following fourth-order equations will be obtained [34, 35]:

$$\begin{cases} \varphi_1^{(iv)}(s) - \dfrac{(m_s + 2m_p)\omega^2}{Y_s I_s + 2Y_p I_p}\varphi_1(s) = 0 \quad ; & 0 < s < L_1 \\ \varphi_2^{(iv)}(s) - \dfrac{m_s\omega^2}{Y_s I_s}\varphi_2(s) = 0 \quad ; & L_1 < s < L_1 + L_2 \\ \varphi_3^{(iv)}(\square\square) - \dfrac{(m_s + 2m_p)\omega^2}{Y_s I_s + 2Y_p I_p}\varphi_3(s) = 0 \quad ; & L_1 + L_2 < s < L_b \end{cases} \tag{32}$$

where $\varphi_i(s)$, *i*=1, 2, and 3, is the mode shape of the *i-th* sub-section. Thus, a partial mode shape can be attributed to each sub-section, and the mode shape of the beam, $\varphi(s)$, is composed of these sub-mode shapes. The mode shapes for sub-sections 1, 2, and 3 are respectively the solutions of Eqs. (32)a, b, and c, which are:

$$\varphi_i(s) = A_i \sin(\lambda_i s) + B_i \cos(\lambda_i s) + C_i \sinh(\lambda_i s) + D_i \cosh(\lambda_i s) \quad ; \quad i = 1, 2, \text{and } 3 \tag{33}$$

where A_i, B_i, C_i and D_i are constants to be determined. In addition, λ_i is the eigenvalue for the *i-th* sub-section mode shape, and is defined as:

$$\lambda_{1,3} = \sqrt[4]{\frac{(m_s + 2m_p)\omega^2}{Y_s I_s + 2Y_p I_p}} \quad ; \quad \lambda_2 = \sqrt[4]{\frac{m_s\omega^2}{Y_s I_s}} \tag{34}$$

Inspecting Eq. (34), one can find that λ_2 and λ_3 relates to λ_1 as:

$$\lambda_2 = \lambda_1 \sqrt[4]{\frac{m_s(Y_s I_s + 2Y_p I_p)}{(m_s + 2m_p)Y_s I_s}} \quad ; \quad \lambda_3 = \lambda_1 \tag{35}$$

Therefore, there are twelve unknown coefficients A_i, B_i, C_i and D_i and one unknown eigenvalue λ_1. To obtain these thirteen unknowns, the geometric boundary conditions at the clamped ends and the continuity of the beam displacement, slope, moment, and shear at the connection points of the sub-sections will be used. Specifically, there are four boundary conditions on the deflection and slope at $s = 0$ and $s = L_b$ along with eight continuity conditions at connection points of the sub-sections and thirteen unknowns. However, as shown later, the remaining unknown will be obtained using the mode shape normalization.

The geometric boundary conditions at $s = 0$ and $s = L_b$ are:

$$\begin{cases} \varphi_1(0) = 0 \\ \varphi_1{}'(0) = 0 \end{cases} \qquad \begin{cases} \varphi_3(L_b) = 0 \\ \varphi_3{}'(L_b) = 0 \end{cases} \tag{36}$$

and the continuity of deflection, slope, moment, and shear at $s = L_1$ and $s = L_1 + L_2$ are:

$$\begin{cases} \varphi_1(L_1) = \varphi_2(L_1) \\ \varphi_1'(L_1) = \varphi_2'(L_1) \\ Y_c I_c \varphi_1''(L_1) = Y_s I_s \varphi_2''(L_1) \\ Y_c I_c \varphi_1'''(L_1) = Y_s I_s \varphi_2'''(L_1) \end{cases} \quad \begin{cases} \varphi_2(L_1 + L_2) = \varphi_3(L_1 + L_2) \\ \varphi_2'(L_1 + L_2) = \varphi_3'(L_1 + L_2) \\ Y_s I_s \varphi_2''(L_1 + L_2) = Y_c I_c \varphi_3''(L_1 + L_2) \\ Y_s I_s \varphi_2'''(L_1 + L_2) = Y_c I_c \varphi_3'''(L_1 + L_2) \end{cases} \tag{37}$$

In Eq. (37), the left and right columns are the continuity conditions at $s = L_1$ and $s = L_1 + L_2$, respectively. The four conditions show the continuity of deflection, slope, moment, and shear, respectively. Now, using the geometric boundary conditions at $s = 0$, which are given in Eq. (36), C_1 and D_1 are written in terms of A_1 and B_1. Thus, $\varphi_1(s)$ is expressed in terms of A_1 and B_1. Next, using the continuity conditions at $s = L_1$, which are given in Eq. (37), the coefficients A_2, B_2, C_2, and D_2 are derived in terms of A_1 and B_1, and consequently, $\varphi_2(s)$ is also written as a function of A_1 and B_1. Finally, using the continuity conditions at $s = L_1 + L_2$, which are also given in Eq. (37), coefficients A_3, B_3, C_3, and D_3, and in turn, $\varphi_3(s)$, are also written in terms of A_1 and B_1. Finally, using $\varphi_3(s)$ and the geometric boundary conditions at $s = L_b$, a system of homogeneous equations, $[\boldsymbol{C}][A_1, B_1]^T = 0$, is obtained. Setting the determinant of matrix $[\boldsymbol{C}]$, which is a transcendental equation, equal to zero, yields the eigenvalue λ_1 and solving one of the equations of this system, gives B_1 in terms of A_1. Therefore, the eigenvalue λ_1 and all the unknown mode shape coefficients except A_1 have been obtained, and $\varphi_1(s)$, $\varphi_2(s)$, and $\varphi_3(s)$, and consequently $\varphi(s)$ are written in terms of A_1. Finally, this remaining constant will be obtained using a normalization condition, which in this research is chosen to be such that the mode shape at midpoint $s = L_b/2$ is set to be one. That is $\varphi(L_b/2) = 1$. Therefore, all the unknowns associated with the sub-section mode shapes are obtained and the mode shape of the beam is uniquely defined. Using the Heaviside functions defined in Eq. (5), the mode shape of the composite beam can be written as:

$$\varphi(s) = \varphi_1(s)H_L + \varphi_2(s)[H(s - L_1) - H(s - L_1 - L_2)] + \varphi_3(s)H_R \quad ; \quad 0 < s < L_b \tag{38}$$

where $H(s)$ denotes the Heaviside function. Now, using Eqs. (31) and (38) in Eqs. (24), pre-multiplying it by $\varphi(s)$, integrating over the beam length, and using Eqs. (31) and (38) in Eq. (30), the following ODEs associated with the PDEs are obtained:

$$\ddot{q} + 2\zeta\omega\dot{q} + \omega^2 q + a_3 q^3 + b_1 q + b_3 q^3 + \theta_b V_s = M_e A_b \sin(\Omega t) \tag{39}$$

$$\frac{C_p}{4}\dot{V}_s + C_{ec}\dot{V}_s = \theta_f \dot{q} \tag{40}$$

where for the sake of simplicity, the dependency of the generalized coordinate q and voltage V_s on time t is not shown. In Eq. (39), ζ, ω, and a_3 are respectively the dimensionless damping ratio, natural frequency, and cubic nonlinearity due to the mid-plane stretching effect. Furthermore, b_1 and b_3 are respectively the contributions of linear and nonlinear parts of the magnetic force. In addition, θ_b is the backward electromechanical coupling, M_e is the modal coefficient of the external excitation, and A_b is the base excitation amplitude. In addition, in Eq. (40), θ_f is the forward electromechanical coupling. The coefficients of these two equations are given in Eq. (A.10) in the Appendix.

Note that, as shown in the Appendix, the backward electromechanical coupling is a scaled version of the forward coupling by the factor $1/M_{eq}$. If the mode shape was mass-normalized, the equivalent mass M_{eq} would be one, and the forward and backward electromechanical couplings would be the same. In addition, both θ_f and θ_b are proportional to $\varphi'_1(s = L_1)$. This shows that if the piezoelectric layers covered the whole length of the beam, due to the clamped boundary condition at $s = L_b$, the electromechanical

couplings would be zero and no electrical energy could be extracted from the beam vibrations. Owing to this reason, for energy harvesting from a doubly-clamped bimorph, the piezoelectric layers must partially cover the beam.

Next, the dimensionless form of the ODEs will be obtained. Hence, the following dimensionless variables are introduced [22, 36]:

$$\bar{q} = \frac{q}{t_s} \;\; ; \;\; \bar{V} = \frac{C_p}{\theta t_s} V_s \;\; ; \;\; \tau = \omega t \;\; ; \;\; x = \frac{s}{L_b} \tag{41}$$

where, $\bar{q}$, $\bar{V}$ and τ are the dimensionless generalized coordinate, voltage, and time, respectively. θ is defined in Eq. (A.10) in the Appendix. In addition, x denotes the dimensionless coordinate, and used to make the mode shape dimensionless, which is denoted by $\bar{\varphi}(x)$. Introducing these parameters into Eqs. (39) and (40), the dimensionless ODEs are obtained as:

$$\bar{q}'' + 2\zeta\bar{q}' + (1+\beta_1)\bar{q} + \beta_3\bar{q}^3 + \Theta\bar{V} = \bar{\Lambda}_b \sin(\bar{\Omega}\tau) \tag{42}$$

$$\frac{\bar{V}'}{4} + C_R\bar{V}' = \bar{q}' \tag{43}$$

In Eqs. (42) and (43), the over-prime shows differentiation with respect to the dimensionless time and the coefficients are defined as:

$$\beta_1 = \frac{b_1}{\omega^2} \;\; ; \;\; \beta_3 = \frac{(a_3+b_3)t_s^2}{\omega^2} \;\; ; \;\; \Theta = \frac{\theta^2}{M_{\text{eq}} C_p \omega^2} \;\; ; \;\; \bar{\Omega} = \frac{\Omega}{\omega} \;\; ; \;\; \bar{\Lambda}_b = \frac{M_e A_b}{\omega^2 t_s} \;\; ; \;\; C_R = \frac{C_{ec}}{C_p} \tag{44}$$

It is worth mentioning that β_1 is the contribution of the linear magnetic stiffness, β_3 is the dimensionless total cubic nonlinearity representing the mid-plane stretching and magnetic nonlinearities, and C_R denotes the dimensionless ratio of the external capacitance to internal (piezoelectric) capacitance. In view of Kirchoff's current law, the right-hand side (RHS) of Eq. (43) can be interpreted as a current source and the first and second terms of the left-hand side (LHS) of Eq. (43) are respectively current passing through one of piezoelectric layers capacitance with capacity of 1/4 and an external capacitance with the capacity of C_R. For numerical simulations, the second term on the LHS of Eq. (43) is multiplied by a Heaviside function to account for forward biased and backward biased actions of the FBR, which are directing or blocking the current towards the FBR based on the instantaneous voltage stored in the external capacitor. If the stored voltage in the capacitor one time step before is lower than the instantaneous voltage, the FBR is forward biased, passes the current and voltage, and adds to the stored voltage in the capacitor. Otherwise, the FBR is backward biased and current generated by the bimorph is blocked by the FBR.

It should be mentioned that in the current approach where the mode shape is scaled to have a maximum value of 1, the dimensionless mode shape $\bar{\varphi}(x)$ at the beam midpoint ($x = 0.5$) is still equal to one, and subsequently, the dimensionless deflection of the beam midpoint is equal to $\bar{q}(\tau)$. Thus, throughout this research, the dimensionless deflection of the beam $\bar{w}$ at its midpoint equals $\bar{q}(\tau)$.

3- Analytical approximation for external capacitor charging time

To assess the charging time of the external capacitor, different assumptions can be adopted. These include:

(1) Considering both the transient time of the response and residual voltage in the capacitor from the previous frequency step
(2) Neglecting the transient time of the response but considering the residual voltage in the capacitor from the previous frequency step
(3) Neglecting the transient time of the response and residual voltage in the capacitor from the previous frequency step

Obviously, among these, option (1) is closer to reality. One can consider that the system starts with an initially empty capacitor at a specific frequency. Furthermore, the transient time can be affected by the system damping, and different cases can be realized for the charging process. In any case, due to the presence of the transient response, no matter if one considers the residual voltage or not, both options (1) and (2) require numerical integration.

On the other hand, as described in what follows, if option (3) is considered, the charging time in the case of steady-state frequency change, although not chirp excitation, can be predicted using an analytical formula. In this case, the open circuit voltage (V_{oc}) can be easily obtained using the HBM solutions. This is not only computationally efficient but also provides a criterion for comparing the charging time regardless of the transient time for different excitation frequencies and amplitudes. To obtain the charging time of the external capacitor under a steady-state change of excitation frequency in accordance with option (3), the dimensionless circuit equation is considered in the following piecewise form:

$$\begin{aligned} &\frac{\bar{V}'}{4} = \bar{q}' && \textit{Reverse biased FBR} \\ &\frac{\bar{V}'}{4} + C_R \bar{V}' = \bar{q}' && \textit{Forward biased FBR} \end{aligned} \tag{45}$$

where the first equation holds true when there is no current flow towards the FBR, and the second equation is valid when current flows towards the FBR. In both of these cases, the RHS of the equation, that is the beam velocity, is indeed a current source. Assuming the beam velocity response as a sinusoidal signal such as $\bar{q}' = \bar{q}_0\, \bar{\Omega} \sin(\bar{\Omega}\tau)$, which is closely in agreement with the HBM response, and using the second equation of Eq. (45) , or equivalently, the current divider rule, the governing equation of the external capacitor current ($\bar{I}_r(\tau)$) can be written as the following piecewise function [37, 38]:

$$\bar{I}_r(\tau) = \begin{cases} 0 & i\pi \le \bar{\Omega}\tau \le r_i \\ \dfrac{4C_R}{1+4C_R} \hat{\bar{I}}_p \,|\sin(\bar{\Omega}\tau)| & r_i \le \bar{\Omega}\tau \le (i+1)\pi \end{cases} \tag{46}$$

Here, the first and second sub-functions govern the reverse and forward biased cases, respectively. In addition, $\bar{\Omega}\tau$ is a scaled time and $\hat{\bar{I}}_p = \bar{q}_0 \bar{\Omega}$ is the amplitude of the current source. Integrating Eq. (45) over the time that no current flows toward the FBR and introducing the change of variable $\bar{\tau} = \bar{\Omega}\tau$, gives:

$$\cos(r_i) = \cos(i\pi) - \frac{\bar{\Omega}}{4\hat{\bar{I}}_p}[\bar{V}(r_i) - \bar{V}(i\pi)] \tag{47}$$

Note that, in odd half-cycles (*i=1, 3, …*) and even half-cycles (*i=2, 4, …*), the following values hold:

$$\begin{cases} \bar{V}(r_i) = -\bar{V}_{\mathrm{c,i}} \\ \bar{V}(i\pi) = \bar{V}_{\mathrm{c,i}} \end{cases} ; \quad i = 1, 3, \ldots \qquad \begin{cases} \bar{V}(r_i) = \bar{V}_{\mathrm{c,i}} \\ \bar{V}(i\pi) = -\bar{V}_{\mathrm{c,i}} \end{cases} ; \quad i = 2, 4, \ldots \tag{48}$$

and for the first even half-cycle (*i=0*), $\bar{V}_{\mathrm{c,i}} = 0$ since there is no voltage initially stored in the external capacitor at the beginning of charging process. Thus, substituting Eq. (48) into Eq. (47) results in:

$$\cos(r_i) = \begin{cases} -1 + \dfrac{\bar{\Omega}\bar{V}_{\mathrm{c,i}}}{2\hat{\bar{I}}_p} & i = 1, 3, 5, \dots \\ 1 - \dfrac{\bar{\Omega}\bar{V}_{\mathrm{c,i}}}{2\hat{\bar{I}}_p} & i = 2, 4, 6, \dots \end{cases} \tag{49}$$

On the other hand, during the external capacitor charging time, integrating the capacitor general equation, $\bar{I}_r(\tau) = C_R \bar{V}_c{}'$ and using the new time scale $\bar{\tau} = \bar{\Omega}\tau$, gives:

$$\int_{r_i}^{(i+1)\pi} \bar{I}_r(\bar{\tau})\, \mathrm{d}\bar{\tau} = \bar{\Omega} C_R [\bar{V}_{\mathrm{c,i+1}} - \bar{V}_{\mathrm{c,i}}] \tag{50}$$

where $\bar{V}_{\mathrm{c,i}} = \bar{V}_c(r_i)$ and $\bar{V}_{\mathrm{c,i+1}} = \bar{V}_c\big((i+1)\pi\big)$.

By integrating the second equation of Eq. (46) and using the new time scale along with Eqs. (49) and (50), one finds:

$$\bar{V}_{\mathrm{c,i+1}} = \bar{A}\bar{V}_{\mathrm{c,i}} + \bar{B} \quad ; \quad \bar{A} = 1 - \frac{2}{1 + 4C_R} < 1 \ \text{ and } \ \bar{B} = \frac{8\hat{\bar{I}}_p}{\bar{\Omega}(1 + 4C_R)} \tag{51}$$

Equation (51) is a recursive equation that relates the external capacitor voltage in the (*i+1)-th* half-cycle to the voltage of the *i-th* half-cycle. Considering that $\bar{V}_{\mathrm{c,0}} = 0$, the recursive equation can be written in the following series form:

$$\bar{V}_{\mathrm{c,i+1}} = \bar{B} \sum_{n=0}^{i-1} \bar{A}^n = \frac{\big(\bar{A}^i - 1\big)\bar{B}}{\bar{A} - 1} \tag{52}$$

As $\bar{A} < 1$, the steady-state voltage of the capacitor, that is obtained by increasing i to a sufficiently large number ($i \to \infty$), is obtained as:

$$\bar{V}_{\mathrm{c},\infty} = \frac{\bar{B}}{1 - \bar{A}} \tag{53}$$

Using the $\bar{A}$ and $\bar{B}$ definitions given in relationship (51), the steady-state voltage of the external capacitor is found to be:

$$\bar{V}_{\mathrm{c},\infty} = 4q_0 \tag{54}$$

On the other hand, using $\bar{q}' = \bar{q}_0\, \bar{\Omega} \sin(\bar{\Omega}\tau)$ in the first equation of Eq. (45), which is the open-circuit equation, and integrating, one finds that:

$$\bar{V} = -\bar{V}_{\mathrm{oc}} \cos(\bar{\Omega}\tau) \quad ; \ \bar{V}_{\mathrm{oc}} = 4\bar{q}_0 \tag{55}$$

where $\bar{V}_{oc}$ is the amplitude of the open-circuit voltage. Thus, the external capacitor voltage at steady-state reaches the open-circuit voltage ($\bar{V}_{\mathrm{c},\infty} = \bar{V}_{\mathrm{oc}}$), where the FBR is reverse biased. This conclusion makes sense, because in steady-state, the external capacitor is full, and no voltage is passed through the FBR. Using this fact, and since the dimensional stored energy in the external capacitor at steady-state is:

$$E_{\mathrm{c},\infty} = \frac{1}{2} C_{\mathrm{ec}} V_{\mathrm{oc}}^2 \tag{56}$$

where V_{oc} is the dimensional open-circuit voltage, the dimensionless energy stored in the capacitor can be written as:

$$\bar{E}_{\mathrm{c},\infty} = \frac{1}{2} C_R \bar{V}_{\mathrm{oc}}^2 \tag{57}$$

By comparing the dimensionless voltage and capacitance ratio in Eq. (57) with their definitions, one can observe that the dimensionless stored energy is related to the dimensional stored energy via:

$$\bar{E}_{\mathrm{c},\infty} = e_r E_{\mathrm{c},\infty} \quad ; \quad e_r = \left(\frac{C_p}{\Theta^2 L_{\mathrm{cr}}^2} \right) \tag{58}$$

where e_r is the coefficient that makes the stored energy dimensionless. Using the recursive equation governing the external capacitor (Eq. (52)), the number of half cycles required to charge the external capacitor to a specific level can be obtained. To do so, consider the desired voltage value to be:

$$\bar{V}_{\mathrm{c,m}} = \bar{B} \sum_{n=0}^{m-1} \bar{A}^m = \frac{(\bar{A}^m - 1)\bar{B}}{\bar{A} - 1} \tag{59}$$

where *m* is the number of the half cycles. Also, consider the ratio of this voltage to the steady-state voltage ($\bar{V}_{\mathrm{c},\infty}$) to be v_R. Thus, based on this requirement and using Eq. (53) along with Eq. (59), the number of half cycles (m) is found to be:

$$m = \frac{\log(1 - v_R)}{\log(1 - \frac{2}{4 + C_R})} \tag{60}$$

Therefore, the number of half cycles depends on the desired voltage level and dimensionless capacitance ratio. Also, Eq. (60) shows that the larger the value of v_R, the higher the number of required half cycles. Furthermore, by increasing the dimensionless capacitance ratio C_R, the number of half cycles increases. This implies that if, according to Eq. (57), the level of stored voltage is increased through increasing C_R, the number of half cycles, and therefore, the time required for charging the external capacitor increase. Finally, to determine the time required to reach the desired voltage level $\bar{V}_{\mathrm{c,m}}$, it should be noted that the time required to complete each half-cycle equals half of the response period. According to the HBM results, the response period equals the excitation period, and it is equal to ($\frac{2\pi}{\bar{\Omega}}$). Thus, the total charging time is the time required to complete *m* half cycles, that is:

$$t_{\mathrm{v_R}} = \frac{m\pi}{\bar{\Omega}} \tag{61}$$

Accordingly, increasing the voltage ratio v_R and/or capacitance ratio C_R, increases the time required to charge the external capacitor. In addition, for fixed values of v_R and C_R, increasing the excitation frequency $\bar{\Omega}$ reduces the charging time.

Multiplying the dimensional work that is given in Eq. (14) by e_r, the dimensionless work required to locate the magnets at specific location is:

$$\bar{W}_T = e_r W_T \tag{62}$$

It should be mentioned that the efficiency of the SPTOS is directly related to the efficiency of the actuation mechanism. Specifically, the above-calculated work required to locate the magnets would be increased if there is any dissipation in the actuation mechanism. However, this does not fundamentally affect the model and indeed its effect can be considered in the required work in Eq. (62) as a greater than one coefficient. Equivalently, its effect can be compensated by multiplying the stored energy in Eq. (57) by a smaller than one coefficient. As this strongly depends on the actuator efficiency and is quite likely to be eliminated to a great extent with a suitable design, in this research, we assume such a dissipation does not exist and all dissipations are considered in the viscous damping. Another practical requirement is that the actuators be non-backdrivable to maintain a prescribed gap when there is no current applied to them. This is quite achievable, as gearboxes can make actuators non-backdrivable or self-locking.

4- Results and discussions

4-1-Simulating the capacitor charging process: steady-state frequency sweep

To examine the electrical response and validate the analysis of Section 3, the electrical response of the circuit will be analyzed using numerical integration for the case of steady-state frequency sweep. To this end, the oscillator velocity $\bar{q}'$, or equivalently the current source, is assumed to be in the following form:

$$\bar{q}' = \bar{q}_0\, \bar{\Omega} \sin(\bar{\Omega}\tau) \tag{63}$$

As the qualitative behavior of the circuit is of interest, the amplitude and frequency of the current source are assumed to be $\bar{q}_0 = 1$ and $\bar{\Omega} = 1$, respectively. Furthermore, to decrease the charging time and make the curves as clear as possible, the capacitance ratio is also assumed to be $C_R = 1$. Using these assumptions, the time histories of the current source or oscillator velocity ($\bar{q}'$), PZT voltage ($\bar{V}$), external capacitor voltage ($\bar{V}_{\mathrm{ec}}$), and current passing through the FBR ($\bar{I}_r$) are given in Fig. 4. In this figure, the border times r_i associated with the forward and reverse biased states are calculated using Eq. (49) and plotted with black dashed lines. In addition, to show the convergence of the PZT and external capacitor voltages into the open circuit voltage, the red horizontal dashed-dotted lines in Fig. 4b and c show the open-circuit voltage amplitude $\bar{\mathrm{V}}_{\mathrm{oc}}$, which equals $4\bar{q}_0$.

According to Fig. 4b, the PZT AC voltage increases from zero and approaches the steady-state amplitude, which as discussed earlier and as shown in the figure, is the open circuit voltage amplitude. Furthermore, based on Fig. 4c, the external capacitor DC voltage, which is positive, increases and it also approaches the steady-state voltage amplitude, in accordance with the discussions in Section 3. Based on Fig. 4b and c, the PZT and external capacitor voltage signals behave differently in the regions $i\pi \leq \bar{\Omega}\tau \leq r_i$ and $r_i \leq \bar{\Omega}\tau \leq (i+1)\pi$, in agreement with the mathematical analysis in Section 3. Specifically, based on Fig. 4c, the slope of the voltage curve in regions where $i\pi \leq \bar{\Omega}\tau \leq r_i$ is constant, and it increases in regions where $r_i \leq \bar{\Omega}\tau \leq (i+1)\pi$, before the steady-state time. This shows that in the former case, the generated voltage does not exceed the already stored voltage in the external capacitor, and thus, the FBR is reverse biased and does not conduct any current. However, in the latter case, the generated voltage by the PZT

layers overcomes the stored voltage in the external capacitor, and the FBR is forward biased and passes the current. The diagram of current passing from FBR that is given in Fig. 4d also shows the FBR current behavior in agreement with the analysis. Specifically, initially, when $0 \leq \bar{\Omega}\tau < \pi$, the capacitor is empty and the FBR is forward biased and passes the current. But when $i\pi \leq \bar{\Omega}\tau \leq r_i$, the FBR is reverse biased and does not conduct any current.

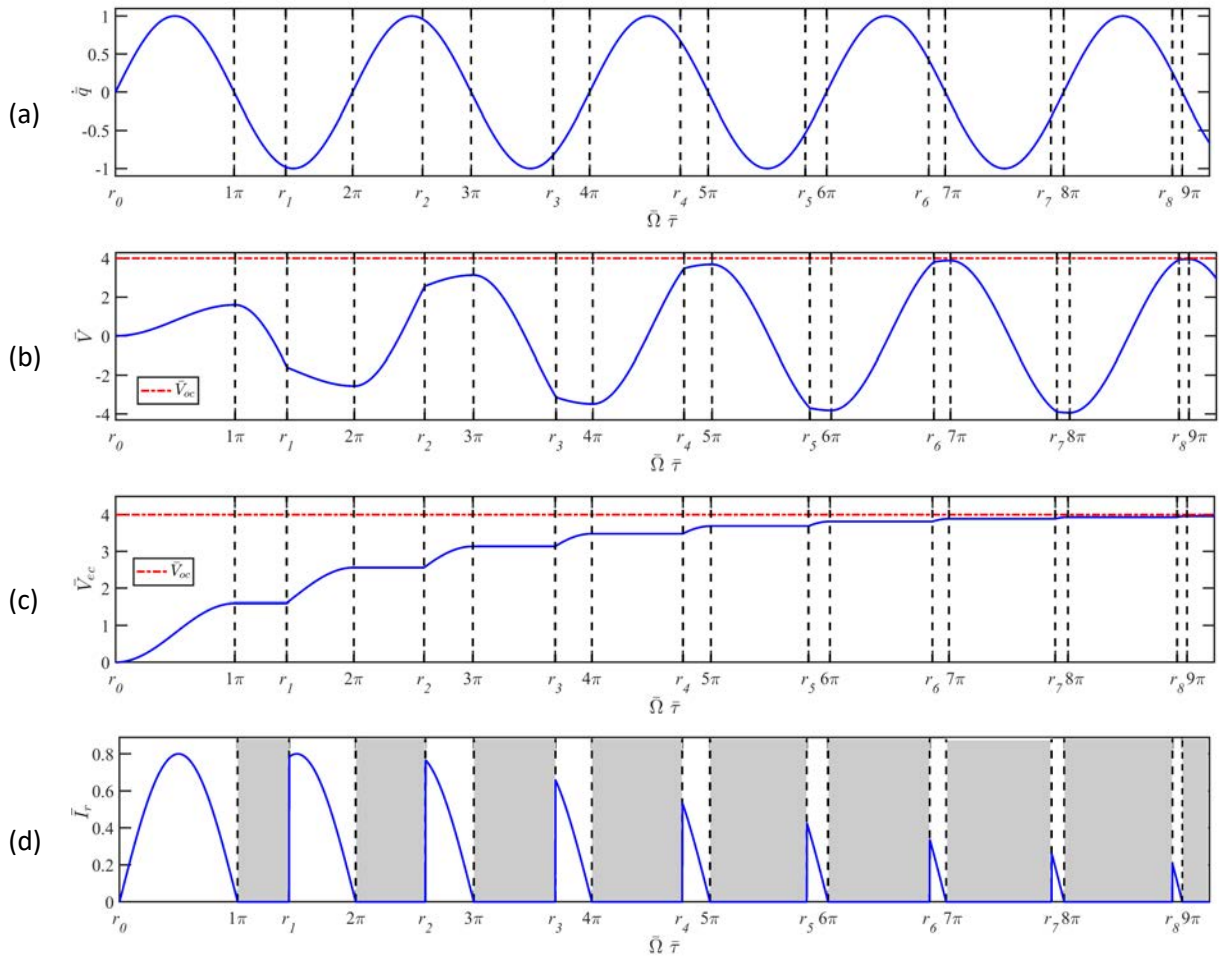

Fig. 4 The time histories of (a) oscillator velocity (b) PZT voltage (c) external capacitor voltage (d) FBR current for $\bar{q}_0 = 1,\ \bar{\Omega} = 1$, and $C_R = 1$

However, when $r_i \leq \bar{\Omega}\tau \leq (i+1)\pi$, the FBR is again forward biased and passes the current towards the external capacitor. Other phenomena that Fig. 4d reveals is that the reverse biased times, that are shown by gray windows, increase gradually. That is, as time passes, the time windows that the FBR conducts current and the capacitor voltage increases become smaller and smaller, and finally approach zero. This can also be seen by comparing the triangle bases in Fig. 4d. Finally, no current passes from the FBR when the steady-state voltage is reached. Another conclusion is that, based on Eq. (60), for $v_R = 0.99$ and $C_R = 1$, the number m is calculated to be 9, and accordingly, 9 half cycles are needed to reach the defined voltage level. As Fig. 4b and c show, the PZT and capacitor voltages almost meet the steady-state voltage line for $m = 9$. These observations show that the mathematical analysis, approximate solution, and arguments, given in Section 3, are in complete agreement with the simulations, and therefore, valid.

Next, to study the effects of the capacitance ratio C_R on the PZT and external capacitor voltages, the stored energy in the capacitor and charging time, the time histories of the PZT voltage, the external capacitor voltage, and the external capacitor energy are given in Fig. 5 for $\bar{q}_0 = 1$ and $\bar{\Omega} = 1$, for three different values of C_R namely 1, 5, and 10. To calculate the charging time, the ratio of voltage is assumed to be $v_R = 0.99$. The scaled charging time ($\bar{\Omega}\bar{\tau}$) associated with each case is shown by the vertical dotted lines. In each figure, the horizontal dotted line shows the steady-state voltage.

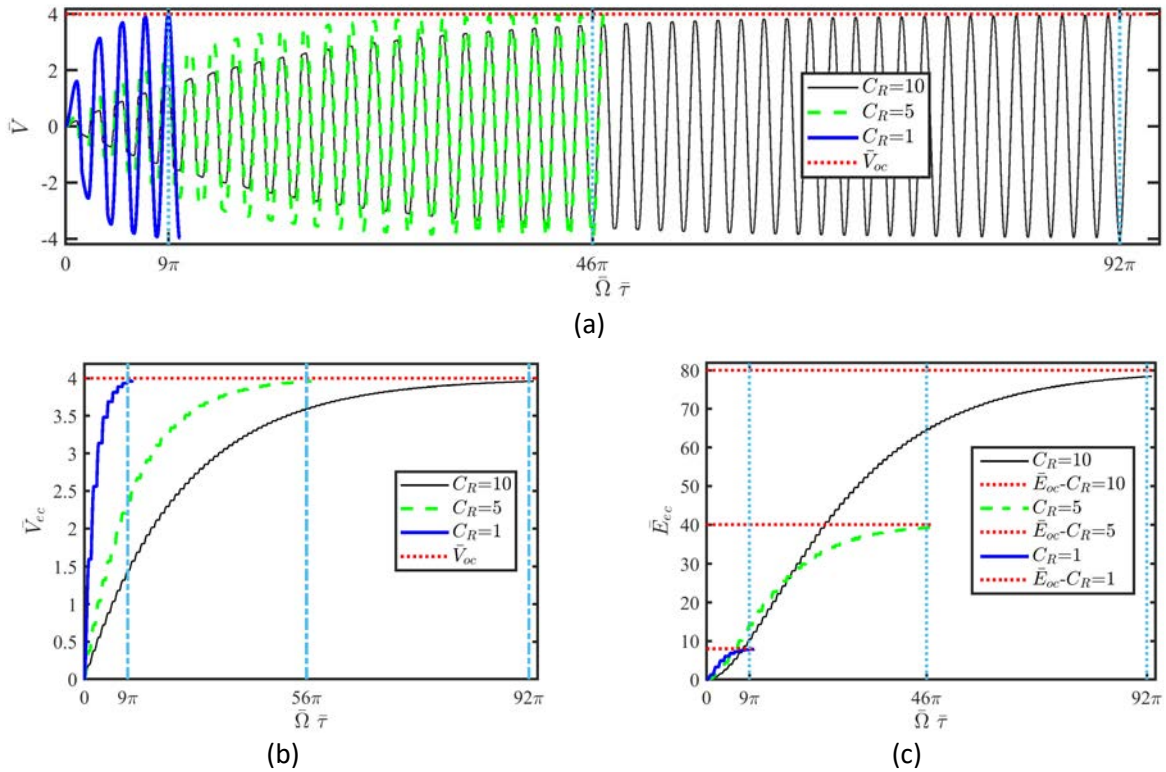

Fig. 5 The time histories of the (a) PZT voltage (b) external capacitor voltage (c) external capacitor energy for $\bar{q}_0 = 1\ and\ \bar{\Omega} = 1$, for $C_R = 1, 5, \text{and } 10$

As shown in Fig. 5a, the PZT steady-state voltage is the same for all cases and equals the open-circuit voltage, as the amplitude and frequency of the input energy to the oscillator are the same, but the charging time increases as C_R increases. Specifically, the scaled charging times for C_R equal to 1, 5, and 10 are 9π, 46π, and 92π, respectively. Likewise, according to Fig. 5b, the external capacitor voltage is also the same as the open-circuit voltage, but the charging time increases as the capacitance ratio increases. However, based on Fig. 5c, the steady-state stored energy in the capacitor increases as the capacitance ratio increases, despite the fact that the input energy to the system is the same. Nevertheless, the time needed to reach the maximum energy, which occurs at the steady-state time, increases as the capacitance ratio increases. Therefore, to increase the stored energy, time is sacrificed.

4-2- SPTOS dynamical response: steady-state frequency sweep

In this section, the SPTOS dynamical response in the case of a steady-state frequency sweep is investigated using both numerical integration and the harmonic balance method (HBM). In order to solve the equations using the HBM, the deflection and voltage of the SPTOS are written as the following series:

$$\bar{q} = a_0 + \sum_{i=1}^{n} a_i \cos(i\bar{\Omega}\tau) + a_{i+1} \sin(i\bar{\Omega}\tau) \tag{64}$$

$$\bar{V} = b_0 + \sum_{j=1}^{n} b_j \cos(j\bar{\Omega}\tau) + b_{j+1} \sin(j\bar{\Omega}\tau) \tag{65}$$

where a_0 and b_0 are the constant terms and a_j and b_j are the coefficients of the *j-th* harmonic. First, in order to obtain the minimum number of required harmonics (*n*) in the HBM solutions, a convergence analysis was conducted. Thus, the frequency response curves of the system dynamical response are plotted for the lower harmonics. Accordingly, the frequency response curves of the oscillator dimensionless midpoint deflection and voltage for the cases of W/O FBR and W/ FBR are shown in Fig. 6, by considering $\bar{\Lambda}_b = 0.1$ and $\zeta = 0.01$ in the two cases of W/O FBR and W/FBR. In the W/O FBR case, $\alpha = 1$ and $m_m = 0$, and for the W/FBR case, $C_R = 1$.

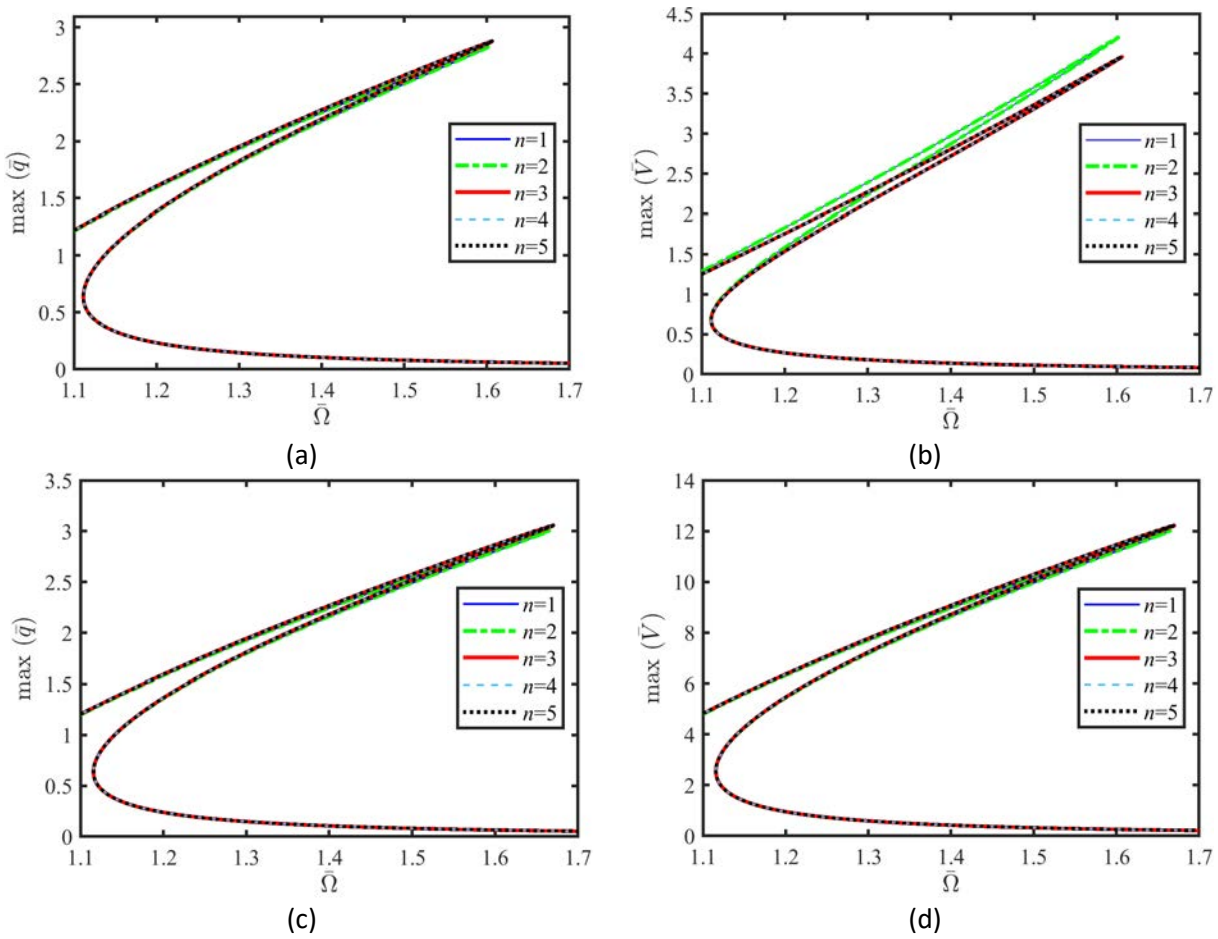

Fig. 6 The frequency response curves of dimensionless (a) midpoint deflection W/O FBR (b) voltage W/O FBR (c) midpoint deflection W/FBR (d) voltage W/ FBR for $\bar{\Lambda}_b = 0.1$ and $\zeta = 0.01$. For the W/O FBR case, $\alpha = 1$ and $m_m = 0$ and for the W/FBR case, $C_R = 1$. In these figures, the curves for n =1 and 2 overlap. Likewise, the curves for n =3, 4, and 5 also overlap.

According to Fig. 6a-d, only considering the fundamental harmonic (*n*=1) in the HBM series cannot predict the system response well in some regions, but for both W/FBR and W/O FBR cases, the frequency response curves of the midpoint deflection and voltage converge for *n*=3. Thus, considering the higher harmonics is necessary to capture the system dynamics correctly, and it what follows, the HBM equations are solved for *n*=3. In addition, the frequency response curves show that the mechanical and electrical responses of the system are of a hardening type, which is due to the midplane stretching induced cubic nonlinearity. This leads to a multi-valued, or here a bi-stable, region in the frequency response curves.

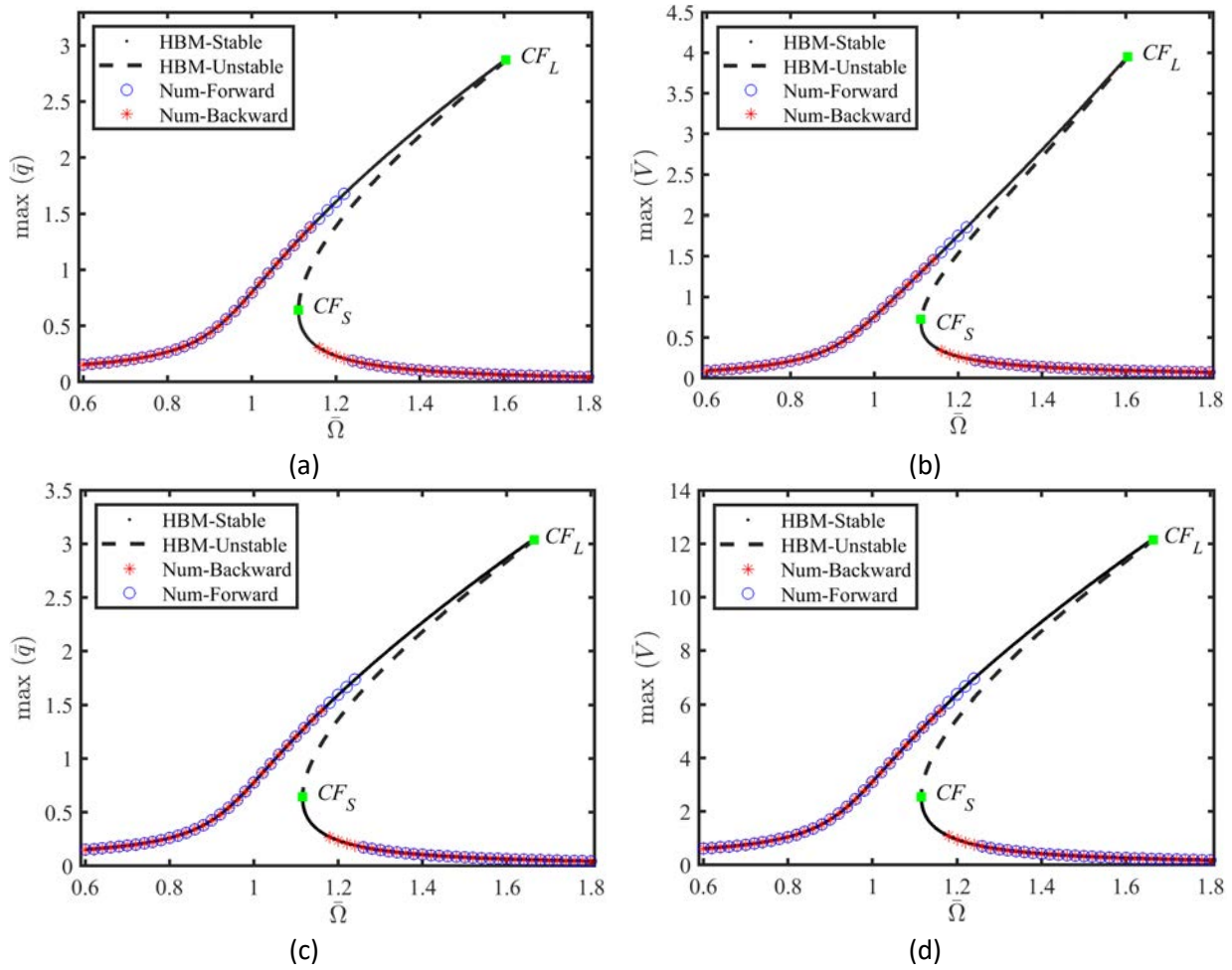

Fig. 7 The numerical- and HMB-based frequency response curves of dimensionless (a) midpoint deflection W/O FBR (b) voltage W/O FBR (c) midpoint deflection W/FBR (d) voltage W/ FBR for $\bar{\Lambda}_b = 0.1$ and $\zeta = 0.01$. For the W/O FBR case, $\alpha = 1$ and $m_m = 0$, and for the W/FBR case, $C_R = 1$

Furthermore, to validate the HBM solutions, the frequency response curves of the dynamical responses for the W/FBR and W/O FBR cases are given in Fig. 7, using numerical integration and the HBM. In the frequency response curves obtained from the HBM, the stable and unstable branches of the solution are shown by solid and broken lines, respectively. Furthermore, the numerical results for forward and backward sweeps are shown by circles and asterisks, respectively. The stability of periodic orbits of the system can be determined by either the Floquet multipliers of the system Monodromy matrix, or equivalently, the eigenvalues of the associated Poincaré map. In this research, the former approach will be used for stability analysis. To this end, a disturbance is superimposed on the periodic orbit of the system and the eigenvalues of the Monodromy matrix are computed. If all the eigenvalues lie inside the unit circle, the periodic orbit is stable and if any of them lies outside the unit circle, the periodic solution is unstable. It should be mentioned that in the open-circuit case, the voltage can be related to the beam deflection via $\bar{V} = 4\bar{q}$. Using this in the mechanical equation, the dimension of the governing equation of the disturbance, and the associated Monodromy matrix will be decreased by one.

As the frequency response curves in Fig. 7 show, the numerical and HBM frequency response curves match very well, which implies that the numerical and HBM solutions are valid. Furthermore, in all frequency response curves in Fig. 7, a jump down phenomenon in the forward sweep path and jump up phenomenon in the backward sweep path are seen in both deflection and voltage frequency response curves using the numerical integration and HBM. These jumps occur at the bifurcation points, leading to dangerous bifurcations, and consequently, multi-valued solutions. By investigating the Floquet multipliers of the Monodromy matrix at the bifurcation points, it is found that a Floquet multiplier leaves the unit circle through +1, leading to a nonhyperbolic periodic solution. In addition, as the frequency response curves of Fig. 7 show, at each bifurcation point, the stable and unstable periodic solutions coalesce and destroy each other. These show the bifurcations are all cyclic-fold type, which is shown by CF. By increasing the excitation frequency, the response experiences a downward jump at the cyclic-fold bifurcation point on the large amplitude branch, shown by CF_L, and is attracted to the low amplitude periodic orbit. On the other hand, by decreasing the excitation frequency, the response experiences an upward jump at the cyclic-fold bifurcation point on the small amplitude branch, shown by CF_S, and is attracted to the large amplitude periodic orbit.

To assess the effects of capacitance ratio and forcing amplitude on the stored energy frequency response curve, the dimensionless stored energy in the capacitor for different capacitance ratios and excitation amplitudes are shown in Fig. 8a and Fig. 8b, respectively. In Fig. 8a, the charging time half-cycle number (m) is also given for each case.

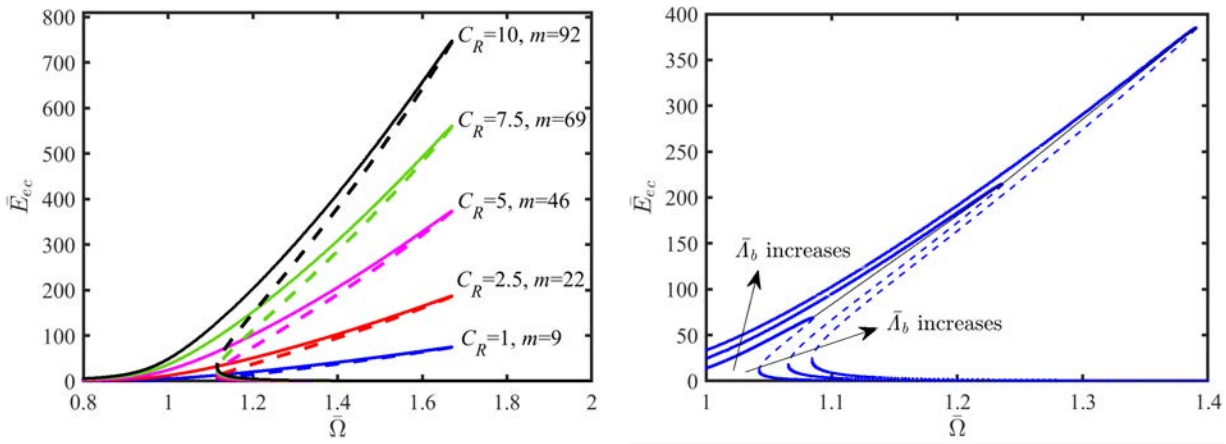

(a) (b)

Fig. 8 The frequency response curves of the stored energy on the external capacitor for different (a) capacitance ratios of $C_R = 1, 2.5, 5, 7.5, and\ 10$ and $\bar{\Lambda}_b = 0.1$ (b) different excitation amplitudes and $C_R = 10$

According to Fig. 8a and Fig. 8b, the stored energy frequency response curves also show a hardening-type behavior, which is expected due to the proportionality of the stored energy to the voltage. Furthermore, based on Fig. 8a, by increasing the capacitance ratio, the stored energy increases considerably, which agrees with Eq. (57). However, the half-cycle number (m) also increases, implying that the higher the energy, the longer the charging time. Specifically, as shown in Fig. 8a, by increasing C_R from one to ten, the stored energy is multiplied by ten, but the half-cycle number increases by about 10 times,

which for a fixed frequency means that the charging time (τ) increases by about ten times. Furthermore, Fig. 8b demonstrates that by increasing the excitation amplitude, the stored energy increases remarkably, and the nonlinear behavior gets intensified, which can be observed by tracing the backbone curve. However, as the capacitance ratio is the same, the increase of energy due to increasing the excitation amplitude does not accompany the increase in the half-cycle number, or equivalently, the charging time. That is, for a fixed excitation frequency, a higher excitation amplitude generates more energy for the same charging time.

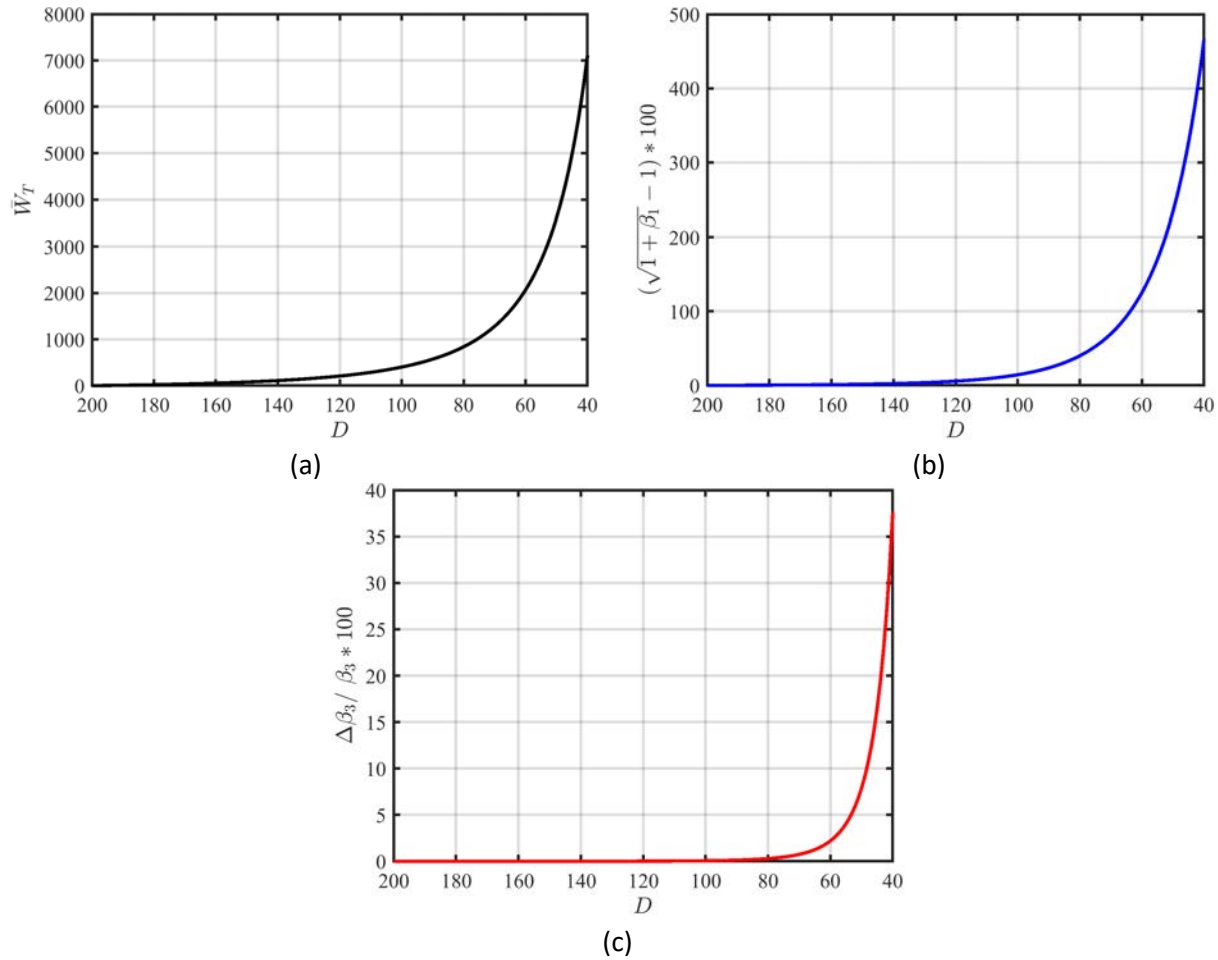

Fig. 9 The curves of (a) required dimensionless magnetic work to locate the external magnets at a specific dimensionless gap D (b) change in the linear natural frequency in percent (c) change in the cubic nonlinearity β_3 in percent versus dimensionless gap value D

It should be mentioned that in the multi-valued regions, where the response experiences jumps, the level of the stored energy depends on which periodic orbit the solution is attracted to. In case the initial conditions are such that the solution is attracted to the low-energy branch, the stored energy is lower than the case the solution is on the high-energy branch. However, for a fixed frequency, the half-cycle number is the same for the small- and large-amplitude periodic orbits.

So far, the dynamics of the oscillator including its deflection, recovered energy, and the behavior of the FBR have been studied. Next, further analyses will be carried out to investigate the viability of the proposed concept, which is to feed the magnetic tuning mechanism with the system vibration energy. First, the required work to move the external magnets from an initial dimensionless position D_0 to a specific dimensionless position D and the accompanying changes in the linear stiffness and nonlinear stiffness of the oscillator will be investigated. In Fig. 9a, b, and c, the variations of the dimensionless work, linear natural frequency of the oscillator, and nonlinear cubic stiffness of the oscillator in percent are shown versus the dimensionless gap value D. Here, the initial gap value is chosen to be large enough such that the magnetic actuation is almost zero. Note that, as the initial gap gives negligible magnetic actuation, the dimensionless linear natural frequency is almost one, and therefore, the variation of the linear natural frequency equals $(\sqrt{1+\beta_1}-1)$.

As Fig. 9a shows, by decreasing the gap value D, the required work to locate the magnets increases. What is sought in this research is to investigate whether the energy recovered from the oscillator vibrations can supply the required work, which is also another type of energy. In addition, based on Fig. 9b, by decreasing the gap, the oscillator natural frequency changes. Specifically, as shown in Fig. 9b, at $D = 107$, the linear stiffness changes by around 10%, and by decreasing the gap value, the stiffness increases monotonically. For example, the SPTOS stiffness changes by 100% for a gap value of $D = 64$. Accordingly, the magnetic actuation can change the oscillator natural frequency and tune it. Likewise, Fig. 9c shows that by decreasing the gap value, the nonlinear cubic stiffness coefficient also increases.

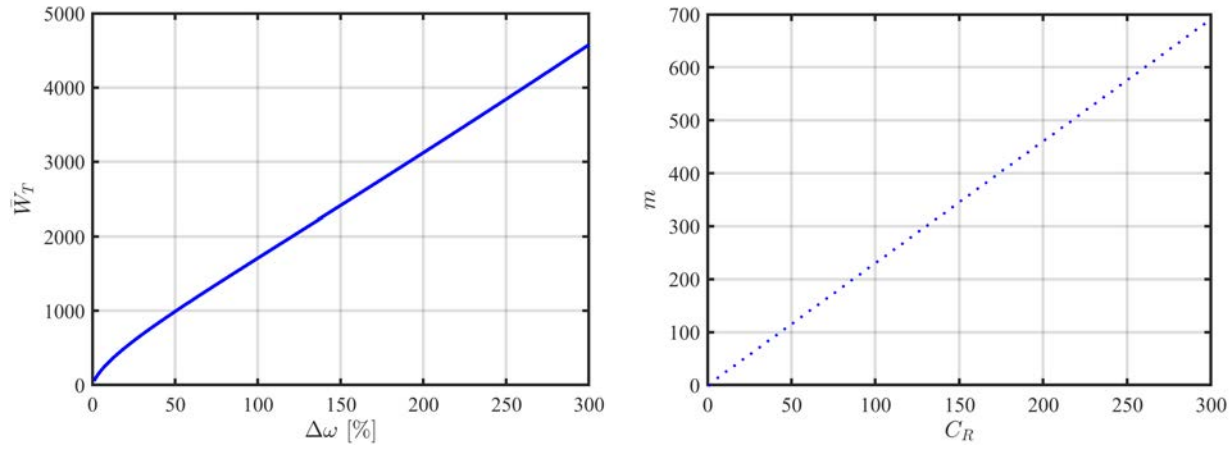

(a) (b)

Fig. 10 The curves of (a) dimensionless magnetic work required to change the oscillator dimensionless natural frequency up to 300% (b) required half-cycle number (*m*) to reach 99% of the steady-state voltage

In Fig. 10a, the magnetic work level required for making a change in the oscillator natural frequency using the magnetic actuation up to 300% is given. In addition, the variations of the half-cycle number (*m*) to charge the external capacitor up to 99% of the steady-state voltage versus the capacitance ratio is shown in Fig. 10b.

Fig. 10a shows that by increasing the dimensionless natural frequency of the oscillator, the required magnetic actuation work also increases. Thus, more energy must be supplied to the tuning mechanism to

locate the frequency at the desired value. On the other hand, Fig. 10b implies that by increasing the capacitance ratio, which increases the stored energy, the half-cycle number (*m*) to reach 99% of the steady-state voltage increases. Therefore, more time is needed to charge the capacitor. This is a trade-off between the stored energy and charging time.

Next, the three-dimensional plots of dimensionless stored energy versus the dimensionless excitation frequency and capacitance ratio are given in Fig. 11, for two different forcing amplitudes of $\bar{\Lambda}_b = 0.1 \text{ and } 0.3$. Furthermore, the work, or equivalently, the energy levels required for some specific values of change in the SPTOS linear natural frequency ($\Delta\omega$) in percent are also shown in Fig. 11 as the horizontal planes. By comparing the stored energy and the work levels, the viability of the proposed concept, which is to power the tuning mechanism via the system harvested energy, can be assessed. In Fig. 11a, the dimensionless capacitance ratio is varied from 20 to 160 and in Fig. 11b, the capacitance ratio is varied from 20 to 100.

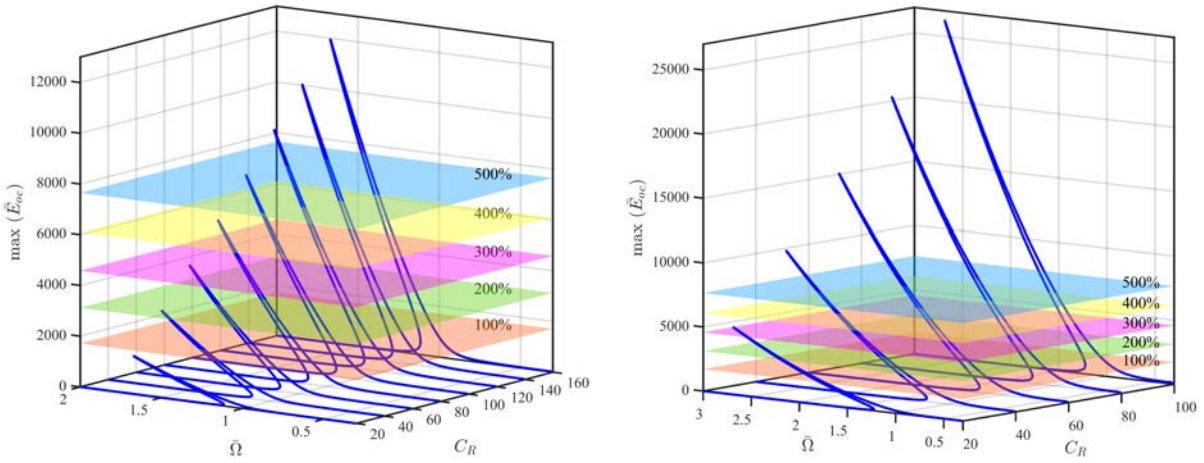

Fig. 11 The three-dimensional plots of dimensionless stored energy versus the dimensionless excitation frequency and capacitance ratio for (a) $\bar{\Lambda}_b = 0.1$ (b) $\bar{\Lambda}_b = 0.3$. In each figure, the horizontal planes show the required work to change the dimensionless linear stiffness by some specific values.

As shown in Fig. 11a, and similar to Fig. 8, the capacitor energy increases by increasing the dimensionless capacitance ratio. Accordingly, for instance when $C_R = 20$, the energy frequency response curve cannot even touch the energy surface corresponding to $\Delta\omega = 100\%$, implying that the oscillator energy is not sufficient to supply the required energy to alter the oscillator frequency by 100%. However, by increasing the capacitance ratio to 40, the energy frequency response curve surpasses the first surface, corresponding to $\Delta\omega = 100\%$, in a frequency range, and therefore, the system energy can be deployed to do work and change the natural frequency by 100%. In a similar manner, by a further increase in the capacitance ratio, the energy frequency response curve touches and surpasses the second surface, which corresponds to $\Delta\omega = 200\%$, for the capacitance ratio of 60. This trend continues, and for instance, for $C_R \geq 120$, the stored energy can supply a change more than $\Delta\omega = 500\%$.

Furthermore, based on Fig. 11b, by increasing the excitation amplitude to $\bar{\Lambda}_b = 0.3$, the stored energy frequency response curve surpasses the $\Delta\omega = 100\%$ plane even for the capacitance ratio of 20, as

opposed to the case of $\bar{\Lambda}_b = 0.1$, for a specific frequency range. That is, the stored energy can supply the required energy to change the oscillator natural frequency by 100%. This is due to the fact that by increasing the excitation amplitude, the deflection, and accordingly, the recovered energy increase. In addition, according to Fig. 11b, by a further increase in the capacitance ratio, the stored energy curve for the capacitance ratio of 40 surpasses the fifth work surface, corresponding to $\Delta\omega = 500\%$. By further increasing the capacitance ratio, the energy frequency response curves surpass $\Delta\omega = 500\%$ by more and over larger frequency regions. Comparing Fig. 11a with Fig. 11b, the minimum capacitance ratio for surpassing the work surface of $\Delta\omega = 500\%$ in the former and latter cases are respectively 120 and 40. That is, the minimum capacitance ratio, for the considered increments for C_R, is decreased by 66.7%, which is remarkable. Thus, by increasing the excitation amplitude, the same energy can be supplied to the magnetic actuator with a smaller capacitance ratio, or equivalently, over a shorter time.

To investigate the effects of capacitance ratio and excitation amplitude on the level of stored energy and surpassing the work levels in a clearer way, the stored energy frequency response curves for different capacitance ratios and the projection of the different required work surfaces on the two-dimensional space are plotted in Fig. 12, for two excitation amplitudes of $\bar{\Lambda}_b = 0.1$ and 0.3. The projected work surfaces are plotted by dashed lines.

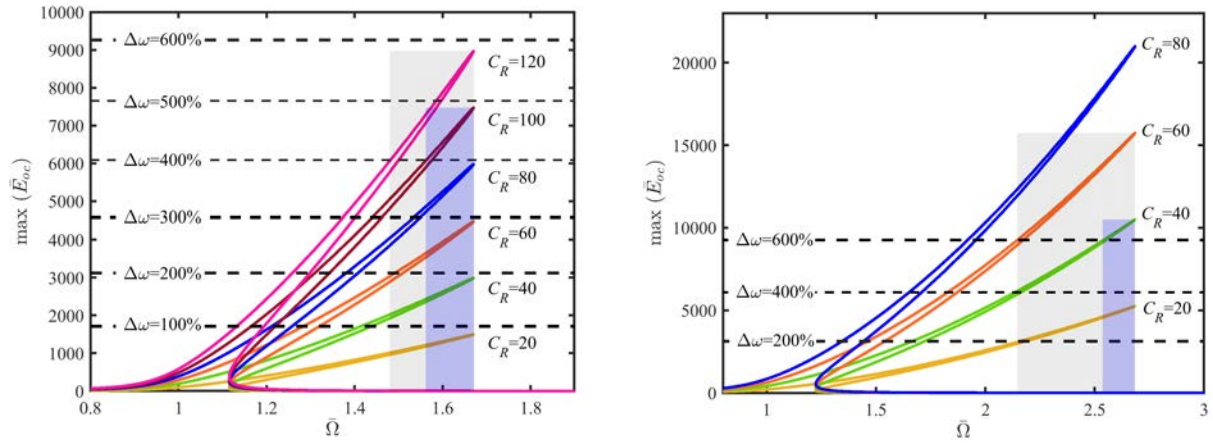

Fig. 12 The frequency response curves of the dimensionless stored energy for different capacitance ratios and two-dimensional projection of the magnetic work levels associated with different linear frequency shifts for (a) $\bar{\Lambda}_b = 0.1$ (b) $\bar{\Lambda}_b = 0.3$

According to Fig. 12a, when the capacitance ratio is 20, the stored energy curve cannot even reach the first work level, associated with a change of $\Delta\omega = 100\%$. However, by increasing the capacitance ratio to $\mathrm{C_R} = 40$, the stored energy curve surpasses the first work level over a specific frequency range, and thus it can supply the required work to change the oscillator natural frequency by 100%. This trend continues by increasing the capacitance ratio, that is, the higher the capacitance ratio, the bigger change in the excitation frequency is possible. Another important point that is implied by Fig. 12a is that, if two energy curves surpass a work level, the one with a higher capacitance ratio exceeds the work level over a larger frequency range. To show this, the frequency ranges over which the frequency response curves corresponding to $\mathrm{C_R} = 100$ and $\mathrm{C_R} = 120$ surpass the fourth work level, associated with $\Delta\omega = 400\%$, are highlighted by the purple and grey rectangles, respectively. The widths of the purple and grey

rectangles are 0.192 and 0.109, respectively, which highlight the expansion of the frequency range surpassing a work level by increasing the capacitance ratio.

Furthermore, based on Fig. 12b, the energy frequency response curve for $\mathrm{C_R} = 20$ even surpasses the work level corresponding to $\Delta\omega = 200\%$, in contrast to the same curve in Fig. 12a, which cannot reach even the work level of $\Delta\omega = 100\%$. Thus, increasing the excitation amplitude can remarkably increase the stored energy and supply the power required by magnetic actuation mechanism for considerable frequency change, even for small capacitance ratios. This stems from larger vibration amplitude due to increased excitation amplitude, which in turn leads to enhanced harvested voltage. By comparing other curves having the same capacitance ratios in Fig. 12a and b, the same trend can be seen. In addition, also in this case, the increase of the capacitance ratio can expand the frequency range over which an energy curve surpasses a specific work level. For instance, the frequency regions in Fig. 12b that the energy curves corresponding to $\mathrm{C_R} = 40$ and $\mathrm{C_R} = 60$ exceed the work level of $\Delta\omega = 600\%$ are highlighted by the purple and grey rectangles, which have the widths of 0.15 and 0.54, respectively.

To study the effects of initial conditions on the periodic attractor, and consequently, the level of stored energy on the external capacitor in multi-valued bistable regions, the oscillator basins of attraction for $\bar{\Omega} = 1.2$ and two excitation levels of 0.05 and 0.1 are shown in Fig. 13a and b, respectively. In addition, the bifurcation set of the oscillator response in the control parameter space of $\bar{\Omega} - \bar{\Lambda}_b$ is given in Fig. 13c. In the bifurcation set, the loci of CF_s and CF_L are shown by dashed and dashed dotted curves, respectively.

In Fig. 13a, where $\bar{\Lambda}_b = 0.05$ and $\bar{\Omega} = 1.2$, the basins of attraction of the small and large periodic attractors are shown by blue and red colors (in gray scale, the red is lighter), respectively. Clearly, the initial conditions determine the attractor to which the response is attracted at steady-state, and therefore, the level of the stored energy. However, for specific values and v_R and C_R, the half-cycle number (m) for charging the capacitor in the basins of attraction of both small and large attractors are the same. Furthermore, in Fig. 13b, where $\bar{\Lambda}_b = 0.1$ and $\bar{\Omega} = 1.2$, the basins of attraction of the small and large periodic attractors are shown by green and black colors (in gray scale, the green is lighter), respectively. Also in this case, the initial conditions still determine the periodic attractor at the steady-state time, and therefore, the level of the stored energy. However, for this excitation level, the size of both small and large attractors, and consequently, their stored energy level must be higher, compared to the previous case shown in Fig. 13a. Here again, the half-cycle numbers for charging the external capacitor for both small and large attractors are the same. It should be mentioned that, although the initial conditions determine the attractor, the level of the stored energy is directly proportional to the capacitance ratio C_R, and for the same attractor, the energy level can be enhanced by increasing C_R. Accordingly, for specific values of v_R and C_R, the time half-cycle numbers in the multivalued region for both small- and large-amplitude orbits are the same, but energy stored for the large-amplitude response will be higher.

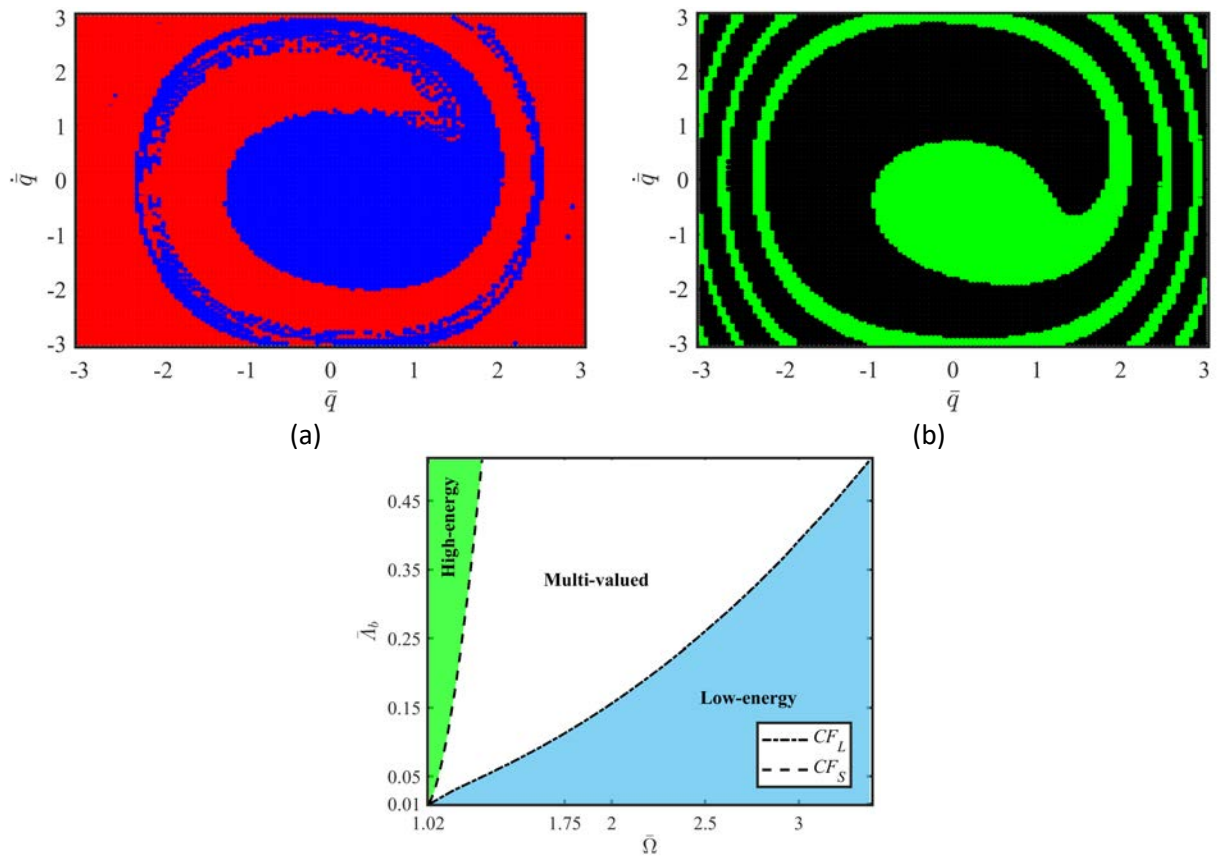

Fig. 13 (a) Basin of attraction for $\bar{\Lambda}_b = 0.05$ and $\bar{\Omega} = 1.2$ (b) basin of attraction for $\bar{\Lambda}_b = 0.1$ and $\bar{\Omega} = 1.2$ (c) bifurcation set in control space for the oscillator W/FBR

Furthermore, in the bifurcation set of Fig. 13c, the green and blue zones show the branches of large- and small-amplitude periodic responses, respectively. Accordingly, the energy of the external capacitor in the former and latter zones are high and low, and thus they are labeled as high-energy and low-energy zones. In addition, the white region is the multi-valued, here bi-stability, region of the response, where both the small- and large-amplitude orbits coexist. The loci of the CF_S and CF_L separate the bifurcation set into different regions. Specifically, if one starts at a point in the green zone and increases the excitation frequency while keeping the excitation amplitude constant, the response amplitude and stored energy of the capacitor increase. Further increasing the excitation frequency and crossing the dashed curve, the oscillator response enters the multi-valued region and can be attracted to either small or large orbits, based on the initial conditions, and the capacitor energy level can be small or large. By a further increase in the excitation frequency while keeping the excitation amplitude constant and crossing the dashed dotted curve, if the response is on the high-amplitude branch, a downward jump occurs and the response is attracted to the low-amplitude orbit, and the capacitor energy drops. Conversely, if one starts in the blue zone and decreases the excitation frequency while keeping the excitation amplitude constant, the oscillator response first enters the multi-valued region through crossing the dashed dotted curve, and then it crosses the dashed curve and moves into the green zone. Also in this case, if the response in the

multivalued region is on the low-amplitude branch, once it passes the dashed line, it jumps upward and is attracted to the high-amplitude branch, which enhances the stored energy on the capacitor.

4-3- SPTOS dynamical response: chirp excitation

Another scenario to consider is a chirp excitation in which the base excitation frequency varies with time. In this case, the dimensionless frequency $\overline{\Omega}$ is assumed to be:

$$\overline{\Omega} = \overline{\Omega}_0 + c\tau \tag{66}$$

where $\overline{\Omega}_0$ is an initial frequency and c is the rate of change of the frequency with time. In sweep up case, $\overline{\Omega}_0$ is assumed to be zero. For each sweep scenario, the sweep time τ is large enough to embrace the multi-valued region.

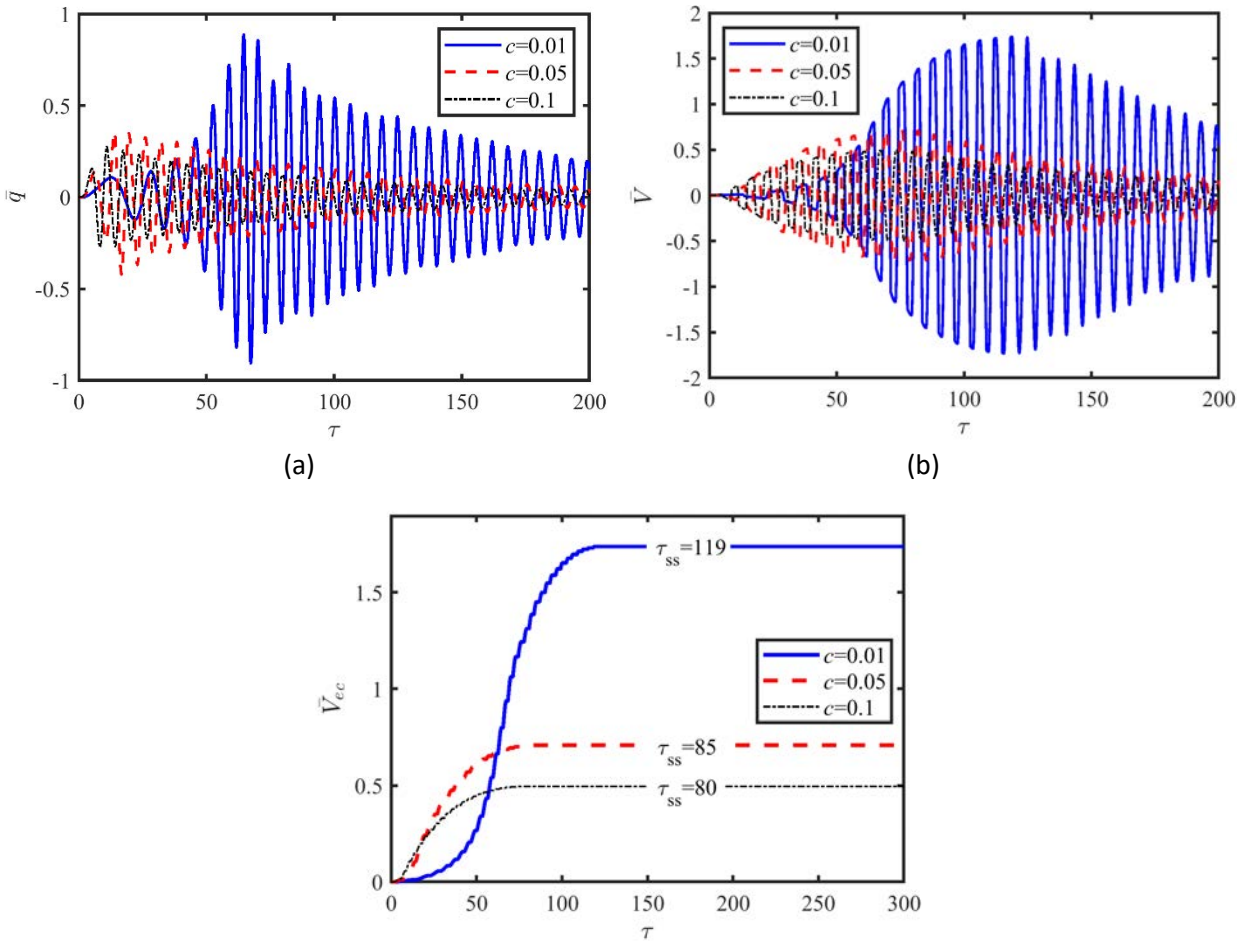

Fig. 14 The time histories of (a) oscillator deflection (b) PZT AC voltage (c) external capacitor DC voltage for $\bar{\Lambda}_b = 0.1$, $C_R = 10$, and three chirp rates of $c = 0.01, 0.05, \text{and } 0.1$

The parameters to be investigated are the sweep rate c and sweep time τ, however, the sweep time is considered large enough to simulate all cases in a fixed time. The time to reach the steady-state energy in the external capacitor under a chirp excitation conforms to index 1, that is it includes both the transient time of the response and residual voltage in the external capacitor from the previous frequency-step.

To investigate the SPTOS response and performance under a chirp excitation, the time histories of the oscillator deflection, piezoelectric AC voltage, and external capacitor DC voltage for a base excitation amplitude of 0.1, an initial frequency of $\bar{\Omega}_0 = 0$, a capacitance ratio of $C_R = 10$, and three sweep rates of $c = 0.01, 0.05, \text{and } 0.1$ are shown in Fig. 14. The total dimensionless chirp time for all three cases is the same and equal to 200.

As shown in Fig. 14a, by increasing the chirp rate, the maximum deflection of the oscillator decreases and occurs at an earlier time. Consequently, based on Fig. 14b, the smaller the chirp rate, the higher the maximum AC voltage of the PZT layers. Accordingly, as shown in Fig. 14c, by decreasing the chirp rate, the maximum voltage of the external capacitor increases, and the time required to achieve the steady-state also increases. Also, as shown in Fig. 14c, the exact steady-state dimensionless times associated with $c = 0.01, 0.05, \text{and } 0.1$ are $\tau_{ss} = 119, 85, \text{and } 80$, respectively. Thus, as for the previous excitation scenario, there is also a trade-off between the energy level and time by changing the chirp rate. The reason for the higher DC voltage for a smaller chirp rate is that the smaller the chirp rate, the higher the AC voltage, therefore, the FBR is reverse biased at higher AC voltage. In addition, the reason behind the decrease of steady-state time by the increase of chirp rate is that, based on Fig. 14b, for a higher chirp rate, the AC voltage reaches its maximum in a shorter time, and therefore, the FBR switches to the reverse biased state earlier. Thus, Fig. 14 shows that the smaller the chirp rate, the higher the external capacitor voltage and steady-state time. From the perspective of supplying the power for a larger actuation force via the magnetic tuning, the chirp rate must be smaller.

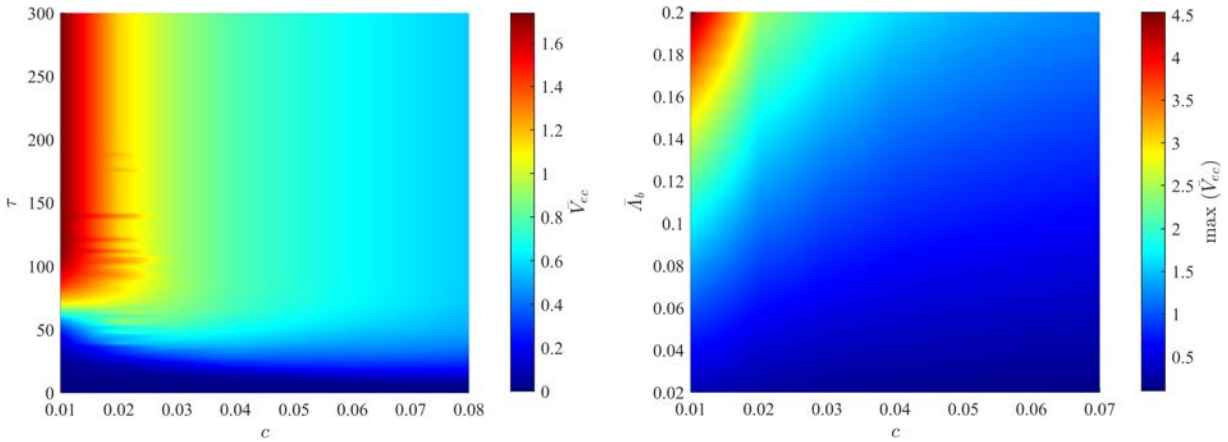

(a) (b)

Fig. 15 The 2D projection of the 3D diagrams of (a) capacitor voltage versus time τ and chirp rate c for $\bar{\Lambda}_b = 0.1$ (b) the maximum of capacitor voltage versus excitation amplitude $\bar{\Lambda}_b$ and chirp rate c for $C_R = 10$

The 2D projection of the 3D curve of external capacitor voltage versus time and chirp rate is shown in Fig. 15a, for $\bar{\Lambda}_{\mathrm{b}} = 0.1$. The 2D projection of the 3D curve of the maximum external capacitor voltage versus the excitation amplitude and chirp rate is given in Fig. 15b.

As Fig. 15a shows, for the excitation amplitude of $\bar{\Lambda}_b = 0.1$, the maximum of capacitor voltage occurs at $c = 0.01$, which is the minimum chirp rate, once the time reaches 121.2. As shown in the figure, by increasing the chirp rate, the maximum of the capacitor voltage and the time required to reach the maximum voltage decrease, and the reasons of these two trends have been explained previously. Furthermore, based on Fig. 15b, the maximum of capacitor voltage increases monotonically with the increase of the excitation amplitude and decrease of the chirp rate. In the considered parameter ranges, the maximum of the capacitor voltage occurs for $\bar{\Lambda}_b = 0.2$ and $c = 0.01$, that is the top left corner of Fig. 15b, because in this case, the oscillator deflection is maximum, and the chirp rate is minimum. However, as explained before, the smaller the chirp rate, the longer is the time required to reach the maximum voltage, which is a trade-off between the maximum voltage of external capacitor and time. In respect of supplying the required energy for magnetic actuation, the higher the required energy, the smaller the sweep rate must be.

So far, it has been found that the external capacitor voltage in the case of chirp excitation depends on the chirp rate. On the other hand, as the previous results show, for the case of a steady-state excitation, external capacitor voltage approaches the open-circuit voltage and does not depend on the capacitance ratio. However, the maximum voltage behavior under a chirp excitation may depend on the capacitance ratio. To investigate this, the 2D projection of the 3D diagrams of the maximum voltage and energy of the capacitor versus chirp rate and capacitance ratio are plotted in Fig. 16a and Fig. 16b, respectively, for the case of $\bar{\Lambda}_b = 0.1$.

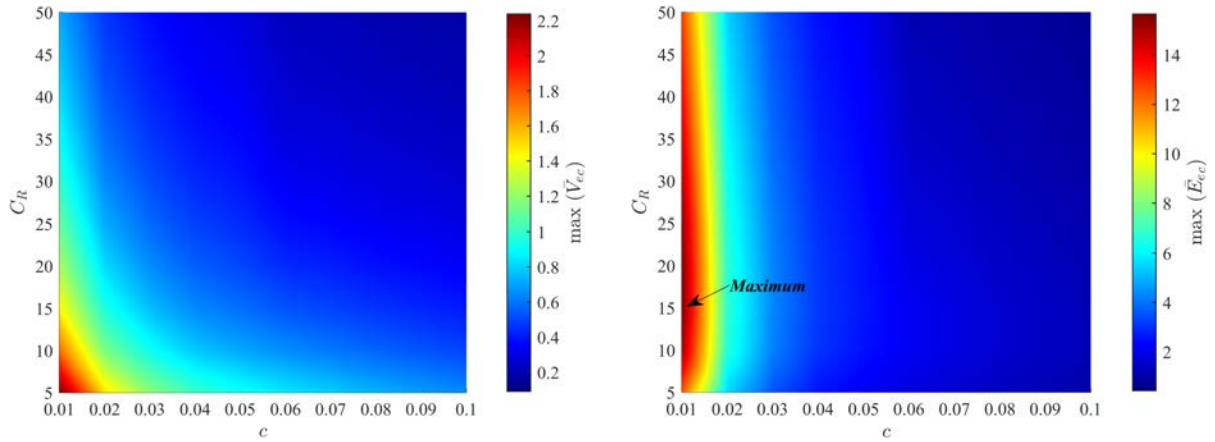

Fig. 16 The 2D projection of the 3D diagrams of the maximum (a) voltage (b) energy of the capacitor versus chirp rate and capacitance ratio for the case of $\bar{\Lambda}_b = 0.1$

As Fig. 16a shows, the maximum of capacitor voltage does vary with both chirp rate and capacitance ratio. This is an underlying difference between two excitation scenarios, because as opposed to the steady-state excitation, the capacitor voltage also depends on the capacitance ratio. For each chirp rate, the maximum

voltage is generated at the minimum capacitance ratio, thus, as shown by in Fig. 16a, the global maximum voltage occurs for the minimum chirp rate and minimum capacitance ratio, which is a point on the bottom left corner of the 2D plot. The reason is that for the minimum chirp rate c, there is enough time for the capacitor to be charged, and meanwhile, the minimum of the capacitance ratio corresponds to the maximum time rate of the voltage. Furthermore, the 2D plot of the maximum energy in Fig. 16b shows that the energy also varies with both chirp rate and capacitance ratio. Indeed, based on Fig. 16b, for any chirp rate, there is a unique capacitance ratio that leads to the maximum energy, which is not the minimum capacitance ratio, as opposed to the voltage results plotted in Fig. 16a. Thus, the trends of variation of voltage and energy with the chirp rate and capacitance ratio are not the same. The global maximum of the capacitor energy in the 2D plane is shown, which is not on the bottom left corner of the plane. Specifically, for the considered parameters, the maximum capacitor voltage 2.24 occurs at $(c = 0.01, C_R = 5)$ while the maximum capacitor energy 15.67 occurs at $(c = 0.01, C_R = 15)$, which shows that the maximum of capacitor voltage and energy are not generated for the same chirp rate and capacitance ratio.

So far, the results show that under a steady-state excitation, the capacitor energy increases linearly with increasing the capacitance ratio, while under a chirp excitation, the energy variation with capacitance ratio is not monotonic. To compare the global maximum energy of the external capacitor under steady-state and chirp excitations, the 2D plot of capacitor energy versus excitation amplitude and capacitance ratio is given in Fig. 17a, considering a chirp rate of 0.01. For the excitation amplitudes of 0.15, 0.2, 0.25, and 0.3, the maxima of the external capacitor energy are shown by the purple markers on the dashed line. The evolution of the maximum energy with the increase of the excitation amplitude can be traced with the dashed line connecting the maximum energy. By increasing the excitation amplitude, both the maximum stored energy and the capacitance ratio corresponding to the maximum energy increase. The frequency response curves of the capacitor energy for the excitation amplitudes of 0.15, 0.2, 0.25, and 0.3 are plotted in Fig. 17b, by considering the capacitance ratio of 15.

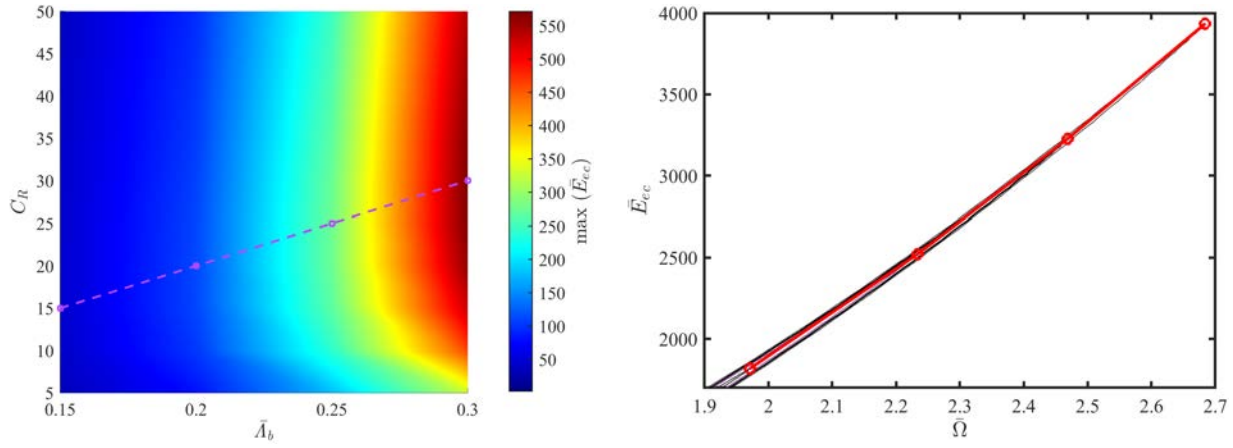

(a) (b)

Fig. 17 The (a) 2D projection of the 3D diagram of the maximum energy of the external capacitor versus the excitation amplitude and capacitance ratio under a chirp excitation and for the chirp rate of $c = 0.01$ (b) frequency response curves of the external capacitor energy for different excitation amplitudes under a steady-state excitation and for the capacitance ratio of $C_R = 15$

This capacitance ratio is the minimum capacitance ratio in the dashed purple line in Fig. 17a, in order to compare the energy of steady-state excitation scenario with the chirp excitation case in the most fair way. The maxima of energy curves can be traced via the backbone curve in Fig. 17b, which is plotted with the red line. Comparing the maxima at points highlighted by circles in both Fig. 17a and Fig. 17b can provide a good insight regarding the efficacy of chirp and steady-state excitations for powering the SPTOS tuning mechanism. To this end, the data of Fig. 17, that include the forcing amplitude, maxima of external capacitor energy, and achievable frequency change, obtained from Fig. 10a, are provided in Table 2.

Table 2. Maximum stored energy in the external capacitor and the work that can be done for steady-state and chirp excitation for $C_R = 15$

	Chirp excitation		Steady-state excitation	
$\bar{\Lambda}_b$	$\max(\bar{E}_{\mathrm{ec}})$	$\Delta\omega$ [%]	$\max(\bar{E}_{\mathrm{ec}})$	$\Delta\omega$ [%]
0.15	44.15	1	1818	108
0.2	111.2	3	2521	157
0.25	275.3	8	3228	207
0.3	571.6	24	3935	256

According to Table 2, the second and fourth columns show that under all considered excitation amplitudes, the maximum of the external capacitor energy for the steady-state excitation is higher than for the chirp excitation. Specifically, under an excitation amplitude of 0.15, the maximum energy under steady-state excitation is approximately 41 times that for the case of chirp excitation. Thus, the achievable frequency changes with the former and latter excitations are 108% and 1%, respectively. Furthermore, under the excitation amplitudes of 0.2, 0.25, and 0.3, the maximum energies of the capacitor under the steady-state excitation are respectively 22.7, 11.7, and 6.88 times the chirp excitation scenario. Consequently, as shown in Table 2, the achievable frequency changes for the excitation amplitudes of 0.15, 0.2, 0.25, and 0.3 under the steady-state excitation are respectively 107, 154, 199, and 232% more than the case of chirp excitation. Therefore, the efficacy of the SPTOS under steady-state excitation is much better than chirp excitation.

To show the effects of applying the magnetic actuation on the oscillator response, the post tuned frequency response curves of the oscillator deflection and external capacitor voltage for two magnetic cases associated with specific frequency changes of 50% and 100% are given in Fig. 18, considering steady-state excitation with $\bar{\Lambda}_b = 0.1$. For comparison, the untuned frequency response curves of the oscillator deflection and voltage are also shown in Fig. 18. In this figure, the linear natural frequency of the system ($\sqrt{1+\beta_1}$) in each case is shown by a dashed dotted line.

As Fig. 18a shows, by locating the external magnets at the dimensionless gap of $\mathrm{D} = 76$, the linear natural frequency of the system ($\sqrt{1+\beta_1}$), which is shown by the dashed dotted line, shifts from 1 to 1.5, that is changed by 50%. Accordingly, the oscillator frequency is tuned using the system energy. Consequently, based on Fig. 18b, the recovered voltage frequency response curve also shifts, as the voltage is a scaled version of the oscillator deflection. On the other hand, Fig. 18c shows that by locating the external magnets at the gap value of $D = 64$, the linear natural frequency of the absorber shifts from 1 to 2, that is it experiences a 100% change. Consequently, as illustrated by Fig. 18d, the recovered voltage frequency response curve also experiences 100% change in the linear natural frequency. Thus, locating the external

magnets closer, the magnetic actuation system can make a bigger change in the oscillator resonance frequency. These results show that SPTOS is a promising concept to use oscillator vibration energy to power the actuation mechanism and realize a self-powered tunable oscillator.

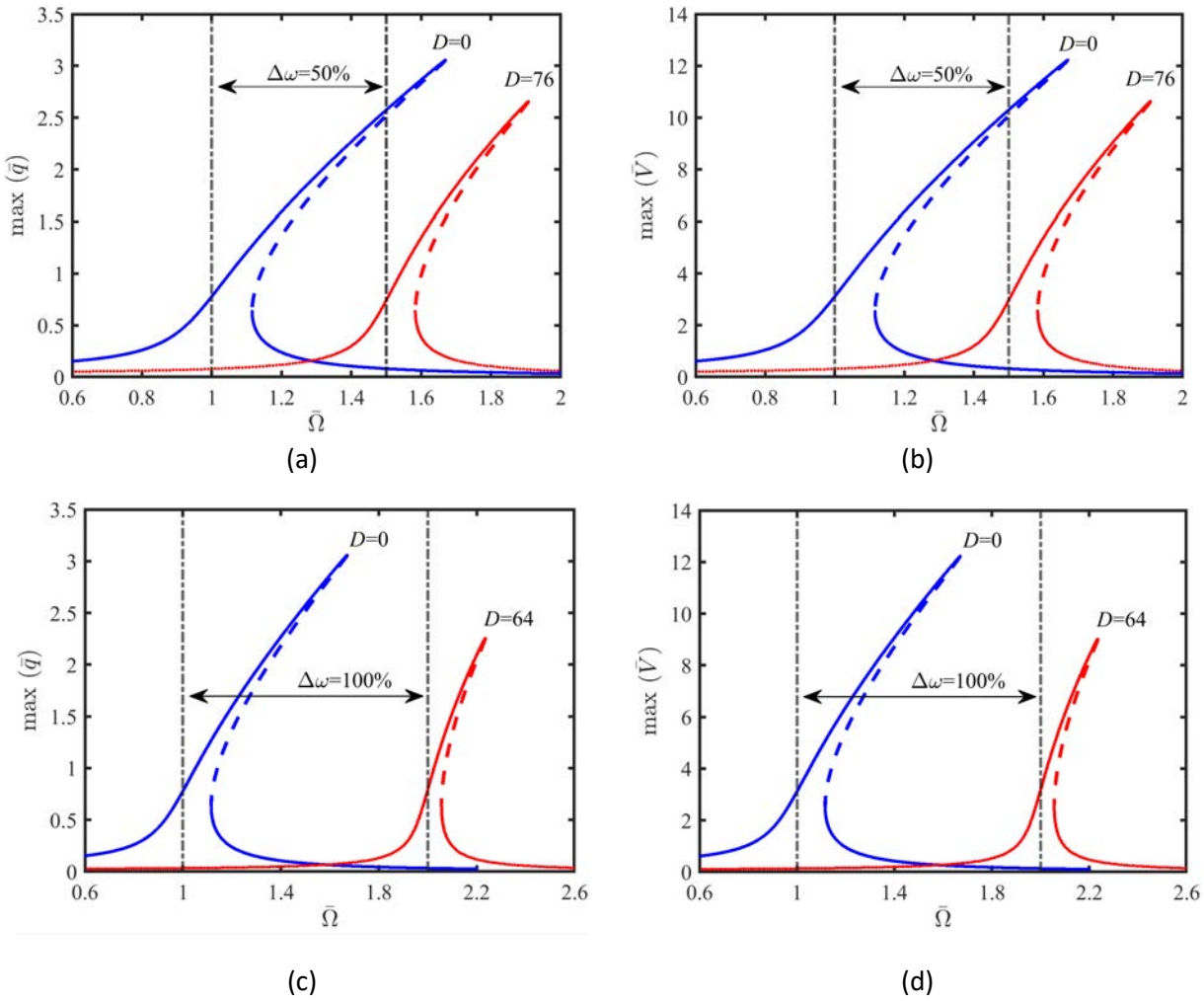

Fig. 18 The frequency response curves of the oscillator (a) deflection for $\Delta\omega = 50\%$ (b) voltage for $\Delta\omega = 50\%$ (c) deflection for $\Delta\omega = 100\%$ (d) voltage for $\Delta\omega = 100\%$ for $\bar{\Lambda}_b = 0.1$

5- Conclusions

In this research, the concept of exploiting oscillator vibration energy to power its frequency tuning mechanism was studied to establish the idea of self-powered tunable oscillators (SPTOS). The proposed system is composed of a doubly-clamped partially covered bimorph piezoelectric beam connected to an electrical circuit with a full bridge rectifier and an external capacitor. Two magnets are attached to the beam, and they interact with two external magnets to provide a magnetic actuation force to tune the

SPTOS resonance frequency. Two different scenarios of steady-state harmonic and chirp base excitations were considered. The dimensionless geometrically nonlinear model of the SPTOS was derived by adopting the extended Hamilton's principle, local displacement fields, and a dipole-dipole magnetic model.

First, the case of steady-state harmonic excitation was considered. Using an approximate-analytical approach to investigate the external capacitor charging process, it was found that the capacitor steady-state voltage reaches the SPTOS open circuit voltage, and this facilitated the analysis in subsequent steps. In addition, the number of half-cycles or charging time, of the capacitor increases with the increase of capacitance ratio, which is the ratio of external and internal capacitances, as well as the ratio of desired voltage to the open circuit voltage. Furthermore, the higher the capacitance ratio, the higher the stored energy at steady-state. Next, the SPTOS response was investigated using the multi-harmonic harmonic balance method (HBM) along with pseudo-arclength continuation. First, the convergence of the HBM was obtained. Then, using stability analysis via Floquet multipliers, cyclic-fold bifurcations in both the SPTOS deflection and open circuit voltage were observed, leading to hardening-type responses and jump up and down phenomena. The validity of the HBM solutions was confirmed via numerical integration.

Furthermore, the dimensionless work levels corresponding to different values of natural frequency changes were obtained and the stored energy was compared with them. It was found that the SPTOS can supply the required energy to tune its natural frequency, through the magnetic actuation, by its own harvested vibration energy. The excitation amplitude, excitation frequency, and capacitance ratio significantly affect the stored energy, and therefore, the extent of possible frequency shifts.

Next, the SPTOS efficacy was investigated under chirp excitation. The results showed that the chirp sweep rate affects the capacitor voltage markedly. Specifically, by decreasing the rate, the stored voltage increases. However, decreasing the rate also increases the charging time. Further investigations showed that by increasing the excitation amplitude, the voltage increases monotonically. Furthermore, for a fixed chirp rate, the maximum voltage occurs for the minimum non-zero capacitance ratio. In addition, as opposed to the steady-state excitation, the maximum energy does not vary monotonically with the capacitance ratio, and the maximum energy was achieved for the minimum chirp rate and a specific capacitance ratio.

To compare the efficiency of the SPTOS for the two excitation scenarios, the maximum energies of the capacitor in these cases were compared and found that the SPTOS energy under steady-state excitation is considerably higher than the case of chirp excitation. Therefore, the SPTOS can supply the energy for larger frequency changes when excited by a steady-state excitation. Finally, the frequency shift of the SPTOS was studied and it was observed that the SPTOS can supply the required energy to change its frequency through magnetic actuation.

Statements & Declarations

Funding

This work was supported by the Research Grants Council (Project No. CUHK14211823), the Innovation and Technology Commission (Project MRP/030/21), Hong Kong Special Administrative Region, China, and The Chinese University of Hong Kong (Project ID: 4055178).

Competing Interests

The authors have no conflicts of interest to declare that are relevant to the content of this article.

Author Contributions

Masoud Rezaei: Conceptualization, Methodology, Software, Investigation, Formal analysis, Validation, Writing – original draft, Writing – review and editing. Michael I Friswell: Methodology, Investigation, Writing – review & editing. Wei-Hsin Liao: Supervision, Investigation, Funding acquisition, Writing – review & editing.

Data Availability

Data sharing is not applicable to this manuscript as no datasets were generated or analyzed during the current study.

Appendix A. Relationships used to derive the nonlinear mathematical model

The displacement components, axial strain, and rotation angle can be related via [23]:

$$e = \sqrt{(1+u')^2 + w'^2} - 1 \quad ; \quad \sin\theta_3 = \frac{w'}{1+e} \quad ; \quad \cos\theta_3 = \frac{1+u'}{1+e} \tag{A.1}$$

where the dependencies of the variables on *s* and *t* are not shown for the sake of simplicity.

The constitutive equation of the substrate layer is:

$$\sigma_{11_s} = Y_s \epsilon_{11} \tag{A.2}$$

The constitutive equations of PZT layers are [39]:

$$\begin{aligned} \sigma_{11_{\mathrm{p1}}} &= Y_p \epsilon_{11} - Y_p d_{31}\left(-\frac{V_s}{4t_p}\right) & \sigma_{11_{\mathrm{p3}}} &= Y_p \epsilon_{11} + Y_p d_{31}\left(-\frac{V_s}{4t_p}\right) \\ \sigma_{11_{\mathrm{p2}}} &= Y_p \epsilon_{11} - Y_p d_{31}\left(-\frac{V_s}{4t_p}\right) & \sigma_{11_{\mathrm{p4}}} &= Y_p \epsilon_{11} + Y_p d_{31}\left(-\frac{V_s}{4t_p}\right) \end{aligned} \tag{A.3}$$

Here, σ_{11} is the axial stress in $\boldsymbol{i_1}$ direction, Y is Young's modulus, and d_{31} is strain constant of PZT layer. In addition, $V_s/4$ shows the voltage generated by each PZT layer in the series connection.

The parameters YA, YI, and θ are defined as:

$$\begin{aligned} YA &= Y_s A_s + 2Y_p A_p [H_L + H_R] \quad ; \quad A_s = W_s t_s \quad ; \quad A_p = W_p t_p \\ YI &= Y_s I_s + 2Y_p I_p [H_L + H_R] \\ \theta &= -2\left(\frac{Y_p d_{31}}{4t_p}\right)\left(\frac{t_s + t_p}{2}\right) W_p t_p [H_L + H_R] \end{aligned} \tag{A.4}$$

The area moment of inertia of the substrate layer I_s and PZT layers I_p are defined as:

$$I_s = \tfrac{1}{12} W_s t_s^3 \quad ; \quad I_p = \tfrac{1}{12} W_p t_p^3 + W_p t_p \left(\tfrac{t_s + t_p}{2}\right) \tag{A.5}$$

The unit vectors of the deformed coordinate system are related to the unit vectors of the undeformed coordinate system using a transformation matrix [T] as:

$$\{\boldsymbol{i_1}, \boldsymbol{i_2}, \boldsymbol{i_3}\}^T = [\boldsymbol{T}]\{\boldsymbol{i_x}, \boldsymbol{i_y}, \boldsymbol{i_z}\}^T \tag{A.6}$$

where the T_{ij} element of the transformation matrix can be extracted using Taylor's expansion as [23]:

$$T_{11} = 1 - \frac{1}{2}w'^2 + u'w'^2 \;\; ; \;\; T_{12} = w' - w'u' + w'u'^2 - \frac{1}{2}w'^3 \;\; ; \;\; T_{13} = 0$$
$$T_{21} = -w' + w'u' - w'u'^2 + \frac{1}{2}w'^3 \;\; ; \;\; T_{22} = 1 - \frac{1}{2}w'^2 + u'w'^2 \;\; ; \;\; T_{23} = 0 \quad \text{(A.7)}$$
$$T_{31} = 0 \;\; ; \;\; T_{32} = 0 \;\; ; \;\; T_{33} = 1$$

Using this transformations matrix, θ_3 can be related to axial strain, $\delta u'$, and $\delta w'$ as [23]:

$$\delta\theta_3 = \frac{T_{21}}{1+e}\delta u' + \frac{T_{22}}{1+e}\delta w' \quad \text{(A.8)}$$

The boundary conditions of the beam:

$$u(0,t) = 0 \;\; ; \;\; u(L_b,t) = 0$$
$$w(0,t) = 0 \;\; ; \;\; w(L_b,t) = 0 \;\; ; \;\; w'(0,t) = 0 \;\; ; \;\; w'(L_b,t) = 0 \quad \text{(A.9)}$$

The coefficients of Eqs. (39) and (40) are:

$$M_{\text{eq}} = \int_0^{L_1}(m_s + 2m_p)\varphi_1^2 \mathrm{d}s + \int_{L_1}^{L_1+L_2} m_s\varphi_2^2 \mathrm{d}s + \int_{L_1+L_2}^{L_b}(m_s + 2m_p)\varphi_3^2 \mathrm{d}s$$

$$\omega = \left[\frac{1}{M_{\text{eq}}}\left[\int_0^{L_1}(Y_sI_s + 2Y_pI_p)\varphi''^2_1 \mathrm{d}s + \int_{L_1}^{L_1+L_2} Y_sI_s\varphi''^2_2 \mathrm{d}s + \int_{L_1+L_2}^{L_b}(Y_sI_s + 2Y_pI_p)\varphi''^2_3 \mathrm{d}s\right]\right]^{\frac{1}{2}}$$

$$a_3 = \frac{\overline{YA}}{2M_{eq}}\left[\int_0^{L_1}\varphi'^2_1 \mathrm{d}s + \int_{L_1}^{L_1+L_2}\varphi'^2_2 \mathrm{d}s + \int_{L_1+L_2}^{L_b}\varphi'^2_3 \mathrm{d}s\right]^2$$

$$b_1 = \frac{12C_m}{M_{\text{eq}}d_v}\varphi_2^2(L_b/2) \qquad ; \quad C_m = \frac{\mu_0 m_1^2}{\pi d_v^4}$$

$$b_3 = \frac{60C_m}{M_{\text{eq}}d_v^3}\varphi_2^4(L_b/2)$$

$$M_e = -[m_s\int_{L_1}^{L_1+L_2}\varphi_2 \mathrm{d}s + (m_s + 2m_p)\left\{\int_0^{L_1}\varphi_1 \mathrm{d}s + \int_{L_1+L_2}^{L_b}\varphi_3 \mathrm{d}s\right\} + 2m_m\varphi_2(L_b/2)]$$

$$\theta_b = \frac{\theta}{\mathrm{M_{eq}}} \;\; ; \;\; \theta = -d_{31}Y_pW_p\left(\frac{t_s + t_p}{2}\right)\varphi'_1(L_1)$$

$$\theta_f = \theta \quad \text{(A.10)}$$

References

[1] G.M. Chatziathanasiou, N.A. Chrysochoidis, C.S. Rekatsinas, D.A. Saravanos, A semi-active shunted piezoelectric tuned-mass-damper for multi-modal vibration control of large flexible structures, J. Sound Vib, 537 (2022) 117222. https://doi.org/10.1016/j.jsv.2022.117222.

[2] M.F. Daqaq, Active shaping of a bi-stable potential: Exploring nonlinear coupling to a stiff externally-excited oscillator, J. Sound Vib, 566 (2023) 117919. https://doi.org/10.1016/j.jsv.2023.117919.

[3] S.R. Anton, H.A. Sodano, A review of power harvesting using piezoelectric materials (2003-2006), Smart Mater. Struct., 16 (2007) R1-R21. https://doi.org/10.1088/0964-1726/16/3/R01.

[4] M.F. Daqaq, R. Masana, A. Erturk, D.D. Quinn, On the role of nonlinearities in vibratory energy harvesting: a critical review and discussion, Appl. Mech. Rev., 66 (2014) 040801. https://doi.org/10.1115/1.4026278.

[5] A. Abdelkefi, Aeroelastic energy harvesting: A review, Int. J. Eng. Sci., 100 (2016) 112-135. https://doi.org/10.1016/j.ijengsci.2015.10.006.

[6] J. Xing, M. Rezaei, H. Dai, W.-H. Liao, Investigating the coupled effect of different aspect ratios and leeward protrusion lengths on vortex-induced vibration (VIV)-galloping energy harvesting: Modelling and experimental validation, J. Sound Vib, 568 (2024) 118054. https://doi.org/10.1016/j.jsv.2023.118054.

[7] C. Chen, L.Y. Chau, W.H. Liao, A knee-mounted biomechanical energy harvester with enhanced efficiency and safety, Smart Mater. Struct., 26 (2017) 065027. https://doi.org/10.1088/1361-665X/aa6cec.

[8] M. Rezaei, R. Talebitooti, M.I. Friswell, Efficient acoustic energy harvesting by deploying magnetic restoring force, Smart Mater. Struct., 28 (2019) 105037. https://doi.org/10.1088/1361-665X/ab3a6a.

[9] W. Chen, J. Mo, J. Zhao, H. Ouyang, A two-degree-of-freedom pendulum-based piezoelectric-triboelectric hybrid energy harvester with vibro-impact and bistable mechanism, J. Energy, 304 (2024) 132143. https://doi.org/10.1016/j.energy.2024.132143.

[10] D. Grzelczyk, M. Wojna, E. Oginska, G. Wasilewski, J. Awrejcewicz, Numerical and experimental investigation of a magneto-electro-mechanical oscillator with a new magnet - coil interaction model and energy harvesting, J. Sound Vib, 583 (2024) 118427. https://doi.org/10.1016/j.jsv.2024.118427.

[11] M.I. Friswell, S.F. Ali, O. Bilgen, S. Adhikari, A. Lees, G. Litak, Non-linear piezoelectric vibration energy harvesting from a vertical cantilever beam with tip mass, J. Intell. Mater. Syst. Struct., 23 (2012) 1505-1521. https://doi.org/10.1177/1045389x12455722.

[12] A. Triplett, D.D. Quinn, The effect of non-linear piezoelectric coupling on vibration-based energy harvesting, J. Intell. Mater. Syst. Struct., 20 (2009) 1959-1967. https://doi.org/10.1177/1045389x09343218.

[13] L.P. Tang, J.G. Wang, Size effect of tip mass on performance of cantilevered piezoelectric energy harvester with a dynamic magnifier, Acta Mech., 228 (2017) 3997-4015. https://doi.org/10.1007/s00707-017-1910-8.

[14] K. Mam, M. Peigney, D. Siegert, Finite strain effects in piezoelectric energy harvesters under direct and parametric excitations, J. Sound Vib, 389 (2017) 411-437. https://doi.org/10.1016/j.jsv.2016.11.022.

[15] K. Khorshidi, M. Rezaeisaray, M. Karimi, Analytical approach to energy harvesting of functionally graded higher-order beams with proof mass, Acta Mech., 233 (2022) 4273-4293. https://doi.org/10.1007/s00707-022-03324-1.

[16] Y.X. Zhang, Y.F. Jin, T.T. Zhang, Dynamical analysis of an asymmetric tri-stable hybrid energy harvesting system driven by colored noise, Acta Mech., 234 (2023) 4391-4406. https://doi.org/10.1007/s00707-023-03615-1.

[17] Y.M. Fan, Y.K. Zhang, M.Q. Niu, L.Q. Chen, An internal resonance piezoelectric energy harvester based on geometrical nonlinearities, Mech. Syst. Signal Process., 211 (2024) 111176. https://doi.org/10.1016/j.ymssp.2024.111176.

[18] M. Bryant, M. Pizzonia, M. Mehallow, E. Garcia, Energy harvesting for self-powered aerostructure actuation, in: Active and Passive Smart Structures and Integrated Systems 2014, SPIE, San Diego, California, United States, 2014, pp. 121-129.
[19] M. Rezaei, R. Talebitooti, Investigating the performance of tri-stable magneto-piezoelastic absorber in simultaneous energy harvesting and vibration isolation, Appl. Math. Model., 102 (2022) 661-693. https://doi.org/10.1016/j.apm.2021.09.044.
[20] M. Rezaei, R. Talebitooti, W.-H. Liao, Exploiting bi-stable magneto-piezoelastic absorber for simultaneous energy harvesting and vibration mitigation, Int. J. Mech. Sci., 207 (2021) 106618. https://doi.org/10.1016/j.ijmecsci.2021.106618.
[21] M. Rezaei, R. Talebitooti, W.-H. Liao, M.I. Friswell, Integrating PZT layer with tuned mass damper for simultaneous vibration suppression and energy harvesting considering exciter dynamics: An analytical and experimental study, J. Sound Vib, 546 (2023) 117413. https://doi.org/10.1016/j.jsv.2022.117413.
[22] M. Rezaei, S.E. Khadem, P. Firoozy, Broadband and tunable PZT energy harvesting utilizing local nonlinearity and tip mass effects, Int. J. Eng. Sci., 118 (2017) 1-15. https://doi.org/10.1016/j.ijengsci.2017.04.001.
[23] A.H. Nayfeh, P.F. Pai, Linear and nonlinear structural mechanics, WILEY-VCH, Weinheim, 2008.
[24] D. Younesian, E. Esmailzadeh, Vibration suppression of rotating beams using time-varying internal tensile force, J. Sound Vib, 330 (2011) 308-320. https://doi.org/10.1016/j.jsv.2010.08.006.
[25] L.Y. Ran, D. Halim, C.K. Thein, M. Galea, Lateral vibration attenuation of a rotor system using an axial control mechanism with resonance detuning, Mech. Syst. Signal Process., 211 (2024) 111220. https://doi.org/10.1016/j.ymssp.2024.111220.
[26] C. Zhang, J. Huang, H. Li, H. Zhou, K. Hu, X. Zhang, H. Tzou, Active vibration control of flexible structures with super-coiled actuators, AIAA J., 62 (2024) 1195-1204. https://doi.org/10.2514/1.J063290.
[27] A. Baz, K. Imam, J. McCoy, Active vibration control of flexible beams using shape memory actuators, J. Sound Vib, 140 (1990) 437-456. https://doi.org/10.1016/0022-460X(90)90760-W.
[28] R.H. Christensen, I.F. Santos, Active rotor-blade vibration control using shaft-based electromagnetic actuation, J Eng Gas Turb Power, 128 (2006) 644-652. https://doi.org/10.1115/1.2056533.
[29] W. Chen, L. Wang, Z. Peng, A magnetic control method for large-deformation vibration of cantilevered pipe conveying fluid, Nonlinear Dyn., 105 (2021) 1459-1481. https://doi.org/10.1007/s11071-021-06662-2.
[30] S.L. Lei, A. Palazzolo, Control of flexible rotor systems with active magnetic bearings, J. Sound Vib, 314 (2008) 19-38. https://doi.org/10.1016/j.jsv.2007.12.028.
[31] P. Li, S.Q. Gao, H.T. Cai, L.S. Wu, Theoretical analysis and experimental study for nonlinear hybrid piezoelectric and electromagnetic energy harvester, Microsyst Technol, 22 (2016) 727-739. https://doi.org/10.1007/s00542-015-2440-8.
[32] M. Zamanian, S.E. Khadem, Analysis of thermoelastic damping in microresonators by considering the stretching effect, Int. J. Mech. Sci., 52 (2010) 1366-1375. https://doi.org/10.1016/j.ijmecsci.2010.07.001.
[33] A.H. Nayfeh, D.T. Mook, Nonlinear oscillations, John Wiley & Sons, New York, 2008.
[34] L. Meirovitch, Analytical methods in vibrations, Macmillan, New York, 1967.
[35] M.A. Koplow, A. Bhattacharyya, B.P. Mann, Closed form solutions for the dynamic response of Euler-Bernoulli beams with step changes in cross section, J. Sound Vib, 295 (2006) 214-225. https://doi.org/10.1016/j.jsv.2006.01.008.
[36] M. Rezaei, R. Talebitooti, Wideband PZT energy harvesting from the wake of a bluff body in varying flow speeds, Int. J. Mech. Sci., 163 (2019) 105135. https://doi.org/10.1016/j.ijmecsci.2019.105135.
[37] W.J. Wu, A.M. Wickenheiser, T. Reissman, E. Garcia, Modeling and experimental verification of synchronized discharging techniques for boosting power harvesting from piezoelectric transducers, Smart Mater. Struct., 18 (2009) 055012. https://doi.org/10.1088/0964-1726/18/5/055012.

[38] M.F. Daqaq, R.S. Crespo, S. Ha, On the efficacy of charging a battery using a chaotic energy harvester, Nonlinear Dyn., 99 (2020) 1525-1537. https://doi.org/10.1007/s11071-019-05372-0.
[39] A. Erturk, D.J. Inman, Piezoelectric energy harvesting, Wiley, Chichester, 2011.